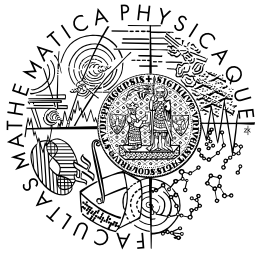

FACULTY
OF MATHEMATICS
AND PHYSICS
Charles University

BACHELOR THESIS

Dominika Hájková

Type of the scheme and tuning dependence of the parameterized orographic gravity wave drag distribution in global climate models

Department of Atmospheric Physics

Supervisor of the bachelor thesis: RNDr. Petr Šácha, Ph.D.

Study programme: Mathematical Modelling

Prague 2022

I declare that I carried out this bachelor thesis independently, and only with the cited sources, literature and other professional sources. It has not been used to obtain another or the same degree.

I understand that my work relates to the rights and obligations under the Act No. 121/2000 Sb., the Copyright Act, as amended, in particular the fact that the Charles University has the right to conclude a license agreement on the use of this work as a school work pursuant to Section 60 subsection 1 of the Copyright Act.

In ..... date ....

Author's signature

I want to thank my supervisor RNDr. Petr Šácha, Ph.D., for all the help and guidance. I would also like to thank Mgr. Aleš Kuchař, Ph.D. for his insight and Roland Eichinger, Ph.D. for his ideas and help with the CMIP6 data.

Title: Type of the scheme and tuning dependence of the parameterized orographic gravity wave drag distribution in global climate models

Author: Dominika Hájková

Department: Department of Atmospheric Physics

Supervisor: RNDr. Petr Šácha, Ph.D., Department of Atmospheric Physics

Abstract: Orographic gravity waves (OGWs) are ubiquitous in the atmosphere and they have an important influence on the dynamics and energy transport especially in the middle-atmosphere. As such, they have to be included in global climate models. Current global models have a low resolution and for that reason OGW effects have to be parameterized. This thesis focuses on the most important output of the OGW parameterizations - the resulting OGW drag. This drag is transported upwards from the surface by the wave and is distributed in the atmosphere. Parameterization schemes differ in many aspects such as the topography description, inclusion of non-linear effects, tuning of the free parameters and others. We have reviewed and described 7 different parameterizations, which are used in 9 different CMIP6 models. After comparing drag data from each of the models we find unexpectedly great differences in the vertical distribution of the drag as well as the magnitude. Focusing on 4 hotspots around the globe, we proposed hypotheses based on the knowledge of the parameterization schemes that can partially explain the inter-model differences. The thesis can pave the way for a more systematic research of the OGW parameterizations in the future, with an ultimate goal of lowering the amount of uncertainty of the future climate projections connected with their parameterized effects.

Keywords: internal gravity waves, parameterizations, global climate models

Contents

Introduction

Orographic gravity waves (OGWs) are atmospheric waves which are sourced by the topography of a planet. They can be depicted as oscillating particles influenced in turns by the buoyant force and gravity. OGWs are ubiquitous in the atmosphere and have a great influence on the dynamics and energy transport. Current global climate models have a low horizontal resolution, mostly order of hundreds of kilometres. Considering that OGWs have horizontal scales from few to thousand of kilometres, global climate models cannot fully resolve them. Solution to that problem is to supplement their effects artificially by the so called parameterizations. Current parameterizations are to a large extent imperfect, however, bear a large influence on the model dynamics [Sacha et al., 2021]. This motivates the ongoing research of OGWs and makes it one of the most lively fields in atmospheric sciences.

The OGW parameterizations influence the models by the resulting drag, which arises as a reaction to the force exerted by the flow on the topography. This drag is not exclusively distributed to the surrounding air masses but it is also transported upwards by OGWs in the form of vertical flux of horizontal momentum, momentum flux in short. It does not change with height, unless the wave dissipates. Then, the drag force is distributed to the ambient wind field where it causes deceleration (or acceleration).

This momentum flux is the main part of the parameterization schemes. There exists a lot of schemes and although they share the basic concepts, they differ in the definition of the momentum flux, formulation and tuning of free parameters and the variety of physical mechanisms considered in addition to the freely propagating OGWs. These differences have a great impact on the magnitude of the resulting drag and its vertical distribution. We can observe these differences especially near the surface and in the middle-atmosphere.

To find out how exactly the drag differs between each model and parameterization we used OGW drag data from CMIP6 - Coupled Model Intercomparison Project Phase 6. We chose 9 models, which employ 7 different parameterizations. We reviewed those parameterizations, comparing their definition of momentum flux and other components. We also attempted to get the information on specific settings of the free parameters in the schemes from the modelers, a unique research effort to date. Then we visualised the data and analysed the differences between the simulations. Finally, we hypothesised the reasons behind the differences in distribution and magnitude of the resulting drag based on the unique information established in the review part of the thesis.

The thesis is structured as follows - in the first chapter we introduce the concept of formation of OGWs and their analytical description. In the second chapter we describe the basics of the OGW parameterization schemes and summarise the relevant information on the schemes from each models. In the third chapter we compare the datasets and describe our hypotheses concerning the intermodel differences. The thesis is concluded by highlighting the need for a follow-up research.

1. Definition of Internal Gravity Waves

Terrestrial atmosphere can be described as a stably stratified fluid for the most part. The stratification constrains vertical motions and supports the existence of wave motions. This thesis concerns the internal gravity waves (GWs), which are ubiquitous across scales in the atmosphere. Sourced by various initial perturbations in the fluid, GWs have important influence on the dynamics, transport and structure in the atmosphere. There are many known sources of GWs, such as orography, convection, frontal systems and various instabilities. In this thesis we focus on orographic GWs (OGWs), created by a flow over some topography.

1.1 Oscillations

GWs can be found in all regions and at all vertical levels in the neutral atmosphere. We can depict them as vertical oscillations of fluid particles. These oscillations are a result of a buoyant force, that acts after a displacement of the particles from equilibrium [Nappo, 2002].

Before we start deriving equation for oscillations in the atmosphere, it is useful to define the potential temperature. It is a temperature that a fluid particle would have, shall we adiabatically displace it from the actual pressure level to a standard pressure level (i.e. $p_0 = 1000\,\mathrm{hPa}$ in the atmosphere). After some thermodynamical considerations [Andrews, 2000] we get

$$\theta = T\left(\frac{p_0}{p}\right)^{\frac{R}{C_p}} = \frac{p}{\rho R}\left(\frac{p_0}{p}\right)^{\frac{R}{C_p}}, \tag{1.1}$$

where R is the gas constant for dry air, C_p is the thermal capacity of dry air at a constant pressure, T and p are the actual temperature and pressure. Potential temperature defined in this way has one obvious and very useful feature, namely, it is a conserved quantity for adiabatic flows.

To derive oscillations of the particles, we will start with the buoyant force that acts on the particles. Let assume that we adiabatically displace one particle from point z_0 to point $z_0 + \delta z$. We assume that the density of that particle remains unchanged during the displacement. However, since it moved to height $z_0 + \delta z$, the density of the surrounding fluid has now value of $\rho(z_0 + \delta z)$.

From Newton's second law we then get

$$\rho_p \frac{\mathrm{d}^2(\delta z)}{\mathrm{d}t^2} = -g(\rho_p - \rho), \tag{1.2}$$

where ρ_p is the density of the particle and ρ is the density of the surrounding fluid. We use the equation of state of dry air $p = \rho RT$ with assumption that the pressure balances much faster than the temperature and density. Therefore, the pressure is the same for the particle as well as the surrounding fluid and we get

$$\frac{\mathrm{d}^2(\delta z)}{\mathrm{d}t^2} = -g\frac{\rho_p - \rho}{\rho_p} = -g\frac{T - T_p}{T}, \tag{1.3}$$

where $T_p(z_0+\delta z)$ and $T(z_0+\delta z)$ are temperatures of the particle and surrounding fluid respectively.

Then another step is expanding temperatures in the nominator into a Taylor series at z_0 up to the first order. Noting, that the first terms of expansions eliminate each other, because of the equal temperature at the height z_0. After omitting higher order terms the result is

$$\frac{\mathrm{d}^2(\delta z)}{\mathrm{d}t^2} = -g\frac{1}{T}\left(\frac{\partial T}{\partial z} - \frac{\partial T_p}{\partial z}\right)\delta z. \tag{1.4}$$

The process of parcel displacement is adiabatic, hence there is no transfer of heat. We can therefore use the first thermodynamical law in terms of enthalpy

$$\delta Q = C_p dT_p - \frac{1}{\rho}dP = 0. \tag{1.5}$$

This can be further manipulated assuming the hydrostatic balance of the ambient atmosphere $\partial p/\partial z = -\rho g$ to get

$$\frac{\partial T_p}{\partial z} = -\frac{g}{C_p}. \tag{1.6}$$

We can use this term for substitution in 1.4

At this point we use potential temperature that we defined in the beginning of this section. We need its derivative and by using hydrostatic equation and the equation of state for dry air again, we express it as

$$\frac{\partial \theta}{\partial z} = \frac{\theta}{T}\left(\frac{\partial T}{\partial z} + \frac{g}{C_p}\right). \tag{1.7}$$

Combining our results from (1.4),(1.6) and (1.7) we arrive at the conclusion that,

$$\frac{\mathrm{d}^2(\delta z)}{\mathrm{d}t^2} = -\frac{g}{\theta}\frac{\partial \theta}{\partial z}\delta z, \tag{1.8}$$

which we recognise as an equation describing harmonic oscillator. Solutions to this equation are very well-known. For the ambient air to support the oscillations of fluid particles and existence of a wave, we need the frequency

$$N = \sqrt{\frac{g}{\theta}\frac{\partial \theta}{\partial z}} \tag{1.9}$$

to be a real number. This points out that GWs can only exist in a stable atmosphere which is described by a positive gradient of the potential temperature with height, which we need for N to be real (and larger than 0). In this case the particle descends to its original place and continues moving up and down due to buoayant and gravitational forces, resulting in an oscillation of the particles within the wave. N is called the Brunt-Väisälä frequency or the buoancy frequency and describes whether the atmosphere is stably stratified ($N^2 > 0$) or unstable, allowing the initial air parcel displacements to be constant or grow with time ($N^2 \leq 0$). We call this convective instability.

The synchronous oscillations of the air parcels are a manifestation of a wave and hence, together with the character of the initial displacement the ambient stability determines the character of the wave.

1.2 Basic description of waves

Waves are usually characterised by a relationship between their spatial and temporal scales, i.e. the dispersion relation, and by polarization relations that describe the projection of the wave into fluctuations of fluid-dynamical variables. We introduce the basic concept in this section. We start with wavelength, which is the distance from one peak, i.e. crest, to another or alternatively from low point, i.e. through, to another. Specifically speaking about GWs, their wavelengths, λ, range from a few to thousands of kilometres in horizontal and tens of metres to kilometres in vertical. It is often convenient to describe the dimension of GWs in terms of a wavenumber

$$\kappa = |\vec{\kappa}| = \frac{2\pi}{\lambda}. \tag{1.10}$$

Using Cartesian coordinate system, wavenumbers in directions x, y and z are called k, l and m respectively. They are defined with wavelengths in each direction, i.e. $\lambda_x, \lambda_y, \lambda_z$. We also define wave vector as $\vec{\kappa} = (k, l, m)$.

Wave period, τ, is the time needed for a wave crest to travel the distance λ, which is also the time it takes the fluid particles to close their trajectories, i.e. exhibit a full oscillation. Angular frequency, ω, is defined as

$$\omega = \frac{2\pi}{\tau} = -\frac{\partial \phi}{\partial t} \tag{1.11}$$

and describes the local change of phase ϕ with time.

In a particular snapshot, waves manifest themselves as a series of lines (curves) with constant phases as seen in Figure 1.1. The wave vector is defined as a gradient of the phase, being always normal to the phase lines.

$$\nabla \phi = \vec{\kappa}. \tag{1.12}$$

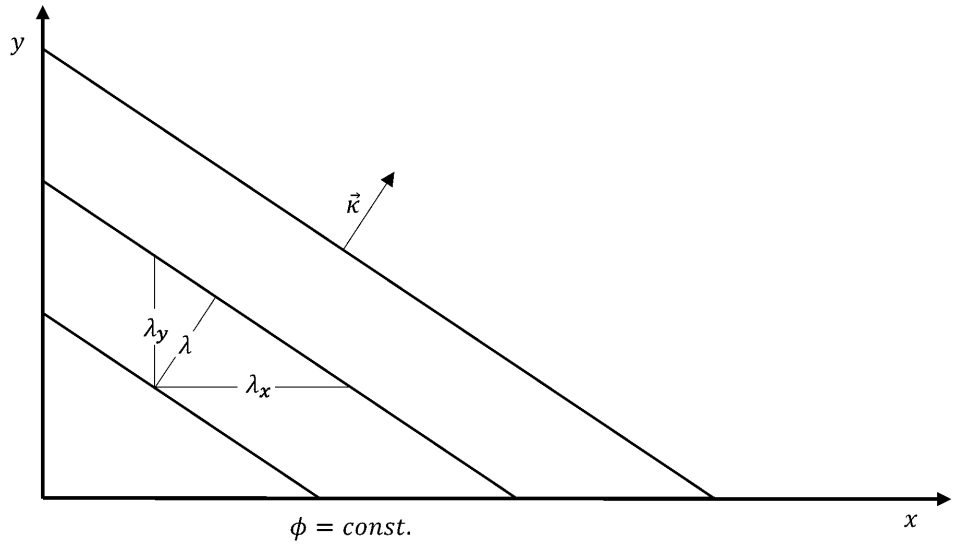

Figure 1.1: Depiction of waves

Using the introduced variables, we can write the phase as

$$\phi(\vec{x}, t) = \vec{\kappa} \cdot \vec{x} - \omega t. \tag{1.13}$$

Then, we can describe the wave field by a general description of a wave

$$\Psi = Re\hat{\Psi}e^{i\phi(\vec{x},t)}, \tag{1.14}$$

where $\hat{\Psi}$ is the amplitude. The rate of the phase propagation is called the phase speed C_k. It is a scalar quantity defined as $C_k = \omega/\kappa$. As we have noted, the phase propagates in the direction of the wave vector, which can be used to define a vector phase velocity. Phase speeds in each direction are defined as $C_{kx} = \omega/k$ and analogously for other components.

It is important that ω may be dependant on κ and that $\omega(\kappa)$ determines the type of the wave. General form of the phase speed may then be described as $C_k(\kappa)$. This relationships are called dispersion relations and the waves where $\omega = \omega(\kappa)$ are called dispersive waves. In summary, dispersion relations describe dependence of the phase speed on the wavelength. Other type of relations that is important for GWs are polarization relations. They are relationships of wave amplitudes, and phases, of different wave variables.

For dispersive waves, it is vital to define another quantity - the group velocity, C_g. To illustrate the meaning and importance of C_g, we have to define a wave packet. Once a wave is formed, it propagates from the source, carrying the energy away. The observed wave is formed of smaller waves with different wavelengths and therefore wavenumbers. The energy that is transported away is distributed between those waves, over a spectrum of wavenumbers. Those smaller waves are enclosed in an envelope and make together a wave packet.

Since the smaller waves have different features, they also have different phase speeds due to dispersion relations. We can also observe that those waves move faster than the packet as a whole. Velocity of the packet is the forementioned group velocity and in x-direction it is defined as

$$C_{gx} = \frac{\partial \omega}{\partial k}. \tag{1.15}$$

As an example we have superposition of two waves with the same amplitude, but slightly different frequency and wavenumber (inspired by an example in Nappo [2002]). In Figure 1.2 one line connects the same peak of the superpositioned waves at different times, the other connects the same node. As we can see by the angles of the lines, waves move faster than the packet as a whole. In the nodes there is a zero amplitude, therefore energy cannot pass through that node and is then carried by the group velocity rather than the phase speeds of the individual waves.

1.3 Linear wave theory

GWs are usually described with a help of linear wave theory and Boussinesq approximation. With this approach we can consequently get dispersion and polarization relations. We will do it following Fritts and Alexander [2003]. We start with a traditional closed set of Euler equations in a rotating frame of reference

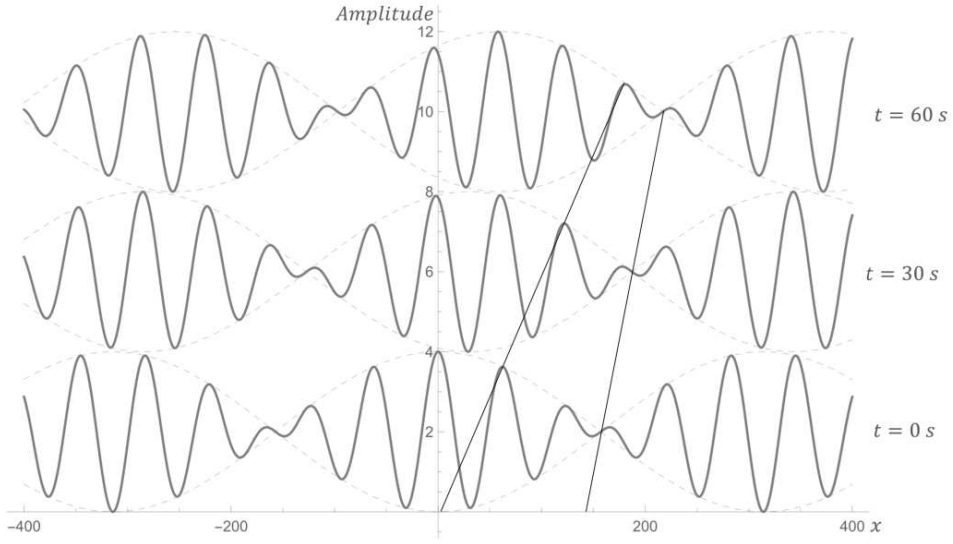

Figure 1.2: Wave packets at different times

in Cartesian coordinates supplemented with a continuity and thermodynamical equation. Those are

$$\frac{Du}{Dt} - fv + \frac{1}{\rho}\frac{\partial p}{\partial x} = F_x, \tag{1.16a}$$

$$\frac{Dv}{Dt} + fu + \frac{1}{\rho}\frac{\partial p}{\partial y} = F_y, \tag{1.16b}$$

$$\frac{Dw}{Dt} + \frac{1}{\rho}\frac{\partial p}{\partial z} + g = 0, \tag{1.16c}$$

$$\frac{D\rho}{Dt} + \rho\nabla \cdot \vec{u} = 0, \tag{1.16d}$$

$$\frac{D\theta}{Dt} = F_p. \tag{1.16e}$$

Equations 1.16a-1.16c are momentum equations in each direction, 1.16d is a mass-continuity equation and 1.16e is the energy conservation showed with the use of conservation of the potential temperature. F_x, F_y, F_p represent external forcings which we will omit in further examination of these equations. f is the Coriolis parameter, $f = 2\Omega \sin\phi$, where Ω is the angular frequency of the Earth and ϕ is in this case latitude. Those equations plus definition of the potential temperature 1.1 make a whole system. We assume

$$\rho = \rho_0 \exp\left(-\frac{z - z_0}{H}\right), \tag{1.17}$$

where ρ_0 is the density at the reference level z_0 and H is a constant parameter representing height scale. D/Dt is the so called material derivative defined as

$$\frac{D}{Dt} = \frac{\partial}{\partial t} + \vec{u} \cdot \nabla. \tag{1.18}$$

Now we use the Boussinesq approximation. This approximation can be used in atmosphere, where we can neglect compressibility in most cases. Under this

approximation sound waves are filtered out of the system. We suppose that density changes are neglectable in all cases except in the buoyancy term. Next step is the Reynolds decomposition of the variables to their mean value and fluctuations. As we said, we assume that the background density changes only with the altitude, which gives us

$$\rho(x, y, z, t) = \overline{\rho}(z) + \rho'(x, y, z, t). \tag{1.19}$$

The decomposition is applied similarly to all the other variables. After that we linearise the equations. By this, we assume that all the variable fluctuations are small, which means we can neglect their and their derivatives squares. With these assumptions, we can modify equations 1.16.

We take normal background wind field defined as $\vec{U} = (\overline{u}(t, z), \overline{v}(t, z), 0)$. With $\overline{w} = 0$, our material derivative will take different form. Since lot of the terms will be omitted by the linearisation, we will see that it is convenient to denote the derivative following way

$$\frac{D}{Dt} = \frac{\partial}{\partial t} + \overline{u}\frac{\partial}{\partial x} + \overline{v}\frac{\partial}{\partial y}. \tag{1.20}$$

Using 1.17 and 1.1 our system of equations is then linearised in this way

$$\frac{Du'}{Dt} + w'\frac{\partial \overline{u}}{\partial z} - fv' + \frac{\partial}{\partial x}\left(\frac{p'}{\overline{\rho}}\right) = 0, \tag{1.21a}$$

$$\frac{Dv'}{Dt} + w'\frac{\partial \overline{v}}{\partial z} + fu' + \frac{\partial}{\partial y}\left(\frac{p'}{\overline{\rho}}\right) = 0, \tag{1.21b}$$

$$\frac{Dw'}{Dt} + \frac{\partial}{\partial z}\left(\frac{p'}{\overline{\rho}}\right) - \frac{1}{H}\left(\frac{p'}{\overline{\rho}}\right) + g\left(\frac{\rho'}{\overline{\rho}}\right) = 0, \tag{1.21c}$$

$$\frac{D}{Dt}\left(\frac{\theta'}{\overline{\theta}}\right) + w'\frac{N^2}{g} = 0, \tag{1.21d}$$

$$\frac{D}{Dt}\left(\frac{\rho'}{\overline{\rho}}\right) + \frac{\partial u'}{\partial x} + \frac{\partial v'}{\partial y} + \frac{\partial w'}{\partial z} - \frac{w'}{H} = 0, \tag{1.21e}$$

$$\frac{\theta'}{\overline{\theta}} = \frac{1}{c_s^2}\left(\frac{p'}{\overline{\rho}}\right) - \frac{\rho'}{\overline{\rho}}. \tag{1.21f}$$

All terms were defined, except c_s, which denotes the speed of sound. We can use it in the system with help of Mayer's formula $C_p = C_v + R$, which we can substitute to the classical definition of the speed of sound in gases and we get

$$c_s = \sqrt{\frac{C_p\overline{p}}{C_v\overline{\rho}}} = \sqrt{\frac{\overline{p}}{(1 - \frac{R}{C_p})\overline{\rho}}}. \tag{1.22}$$

Where R/C_p is a familiar term in the definition of the potential temperature.

Next step is the WKB approximation. This method lies in assuming $\overline{u}, \overline{v}$ and N to be only slowly changing in the vertical. This means omitting more terms

in 1.21a and in 1.21b. We also assume, that we can express the wave solutions to this system as

$$\left(u', v', w', \frac{\theta'}{\overline{\theta}}, \frac{p'}{\overline{\rho}}, \frac{\rho'}{\overline{\rho}}\right) = (\tilde{u}, \tilde{v}, \tilde{w}, \tilde{\theta}, \tilde{p}, \tilde{\rho}) \cdot \exp\left[i(\vec{k} \cdot \vec{x} - \omega t) + \frac{Z}{2H}\right], \tag{1.23}$$

where terms with a tilde represent amplitudes of each variable and ω is in this case Eulerian, so the observed frequency. We can also define the intrinsic frequency $\hat{\omega} = \omega - k\overline{u} - l\overline{v}$, which will appear after substituting solution 1.23 to our system 1.21. Then we get

$$-i\hat{\omega}\tilde{u} - f\tilde{v} + ik\tilde{p} = 0, \tag{1.24a}$$

$$-i\hat{\omega}\tilde{v} + f\tilde{u} + il\tilde{p} = 0, \tag{1.24b}$$

$$-i\hat{\omega}\tilde{w} + \left(im - \frac{1}{2H}\right)\tilde{p} = -g\tilde{\rho}, \tag{1.24c}$$

$$-i\hat{\omega}\tilde{\theta} + \left(\frac{N^2}{g}\right)\tilde{w} = 0, \tag{1.24d}$$

$$-i\hat{\omega}\tilde{\rho} + ik\tilde{u} + il\tilde{v} + \left(im - \frac{1}{2H}\right)\tilde{w} = 0, \tag{1.24e}$$

$$\tilde{\theta} = \frac{\tilde{p}}{c_s^2} - \tilde{\rho}. \tag{1.24f}$$

These equations can be combined to make one equation only. To find this equation, it is easiest to portray this system as a matrix with amplitudes as solutions for a trivial right hand side as shown in Procházková [2021]. With this we get a condition that determinant must be equal to 0 to get a non-trivial solution. After we get the determinant, we want both the real and the imaginary part of it to be zero and this yields respectively

$$\frac{g}{c_s^2} = \frac{1}{H} - \frac{N^2}{g}, \tag{1.25a}$$

$$\hat{\omega}\left(k^2 + l^2 + m^2 + \frac{1}{4H^2} - \frac{(\hat{\omega}^2 - f^2)}{c_s^2}\right) = N^2(k^2 + l^2) + f^2\left(m^2 + \frac{1}{4H^2}\right). \tag{1.25b}$$

The condition resulting from the imaginary part is already modified by the condition from the real part. We do not want to account for the sound waves, so we assume they spread with infinite speed, so that $c_s \to \infty$. This filters out the sound waves and we end up with the dispersion relation for gravity waves

$$\hat{\omega}^2 = \frac{N^2(k^2 + l^2) + f^2\left(m^2 + \frac{1}{4H^2}\right)}{k^2 + l^2 + m^2 + \frac{1}{4H^2}}. \tag{1.26}$$

We can also derive relation for the vertical wavenumber m, which will show us more about the bounds of $\hat{\omega}$

$$m^2 = \frac{(k^2 + l^2)(N^2 - \hat{\omega}^2)}{\hat{\omega}^2 - f^2} - \frac{1}{4H^2}. \tag{1.27}$$

We assume vertical propagation of the waves with no decaying of the amplitude, therefore the wavenumbers are real (and non-zero). This gives us that both the left-hand side and the right-hand side of the equation are positive. Since in stable atmosphere N^2 is usually greater than f^2, this gives us condition $N^2 > \hat{\omega}^2 > f^2$. This tells us, that although the spectrum of GWs can be quite large, the frequency is always less than the Brunt-Väisälä frequency.

Another quantity we can derive is the group velocity. As it is the group velocity that transports energy, it has an important part in the description of GWs. We derive it by following the definition 1.15. Using $\hat{\omega} = \omega - k\overline{u} - l\overline{v}$ we modify the left-hand side of 1.26 and express ω, with assumption that it is positive. After differentiation we get

$$\begin{aligned}(c_{gx}, c_{gy}, c_{gz}) = \left(\frac{\partial\omega}{\partial k}, \frac{\partial\omega}{\partial l}, \frac{\partial\omega}{\partial m}\right) = \\ (\overline{u}, \overline{v}, 0) + \frac{[k(N^2 - \hat{\omega}^2), l(N^2 - \hat{\omega}^2), -m(\hat{\omega}^2 - f^2)]}{\hat{\omega}\left(k^2 + l^2 + m^2 + \frac{1}{4H^2}\right)}.\end{aligned} \tag{1.28}$$

Finally, we can also derive the polarization relations. Since a polarization relation can be any relation between 2 different amplitudes of wave variables, we can derive many of them, noting that we have already derived 1.26. We point out some of the most important ones

$$\tilde{u} = \left(\frac{i\hat{\omega}k - fl}{i\hat{\omega}l + fk}\right)\tilde{v}, \tag{1.29a}$$

$$\tilde{p} = \left(\frac{\hat{\omega}^2 - f^2}{\hat{\omega}k + ifl}\right)\tilde{u} = \left(\frac{\hat{\omega}^2 - f^2}{\hat{\omega}l - ifk}\right)\tilde{v}, \tag{1.29b}$$

$$\tilde{w} = \frac{\left(m - \frac{i}{2H}\right)\hat{\omega}}{N^2 - \hat{\omega}^2}\tilde{p}. \tag{1.29c}$$

1.4 Orographic gravity waves and drag

As mentioned in the previous part, synchronous vertical movement of air particles may lead to sourcing of waves (and is a manifestation of their propagation). This can occur in cases of air flowing over some topography such as mountains or hills. Horizontal scales of the resulting OGWs largely reflect the scales of the topography, from few to thousands of kilometres, and have vertical wavelengths from a few to tens of kilometres. OGWs are able to propagate both horizontally and vertically, being able to transfer energy and momentum from the surface to the free atmosphere.

Let us assume a stably stratified flow over some pronounced terrain, for example a mountain ridge. When advected parcels arrive to the ridge, they exert pressure on the wind-facing slope of the ridge, and, as described by the Newton's third law, the ridge exerts an equal but opposite force on the incident parcels. As a result, the parcels are displaced out of their initial equilibrium positions in the flow and depending on the properties of the flow and the force, OGWs may form and propagate away from the topography. The horizontal phase speed and

frequency of the wave measured by a static observer would be zero. In a reference frame moving with the background flow, the intrinsic phase speed of the wave would be therefore negative and of a similar magnitude as the background wind velocity.

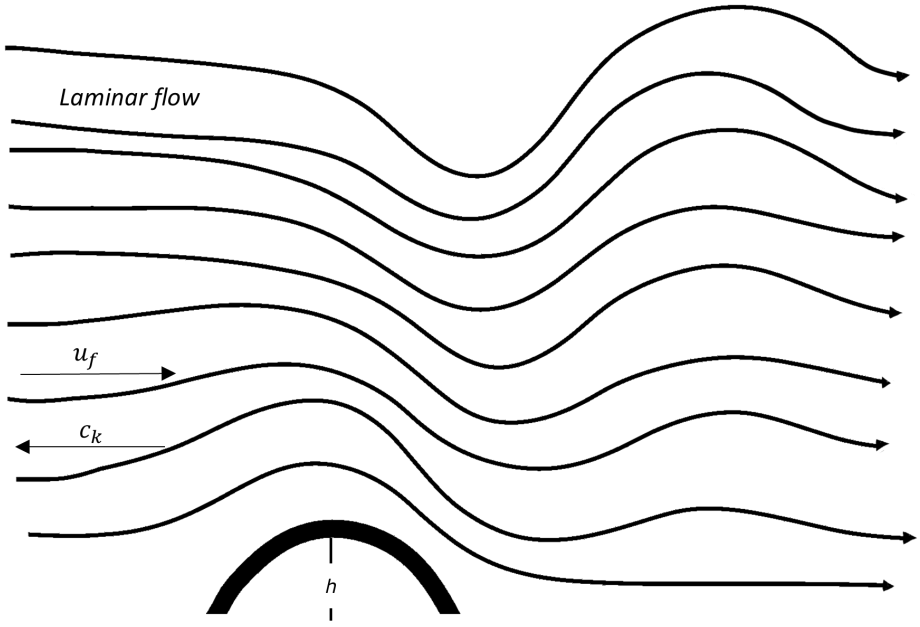

Figure 1.3: Illustration of flow with velocity u_f and resulting formation of OGWs with intrinsic phase speed C_k

The process of OGW formation is depicted in the Figure 1.3. The influence of the orography on the flow has a form of a frictional force known as a form drag force (or pressure drag). We can directly estimate its overall strength as

$$D = \int_0^{\lambda} p \frac{\mathrm{d}h}{\mathrm{d}x} \, \mathrm{d}x = - \int_{-\frac{l}{2}}^{\frac{l}{2}} \overline{\rho} u' w' \, \mathrm{d}x, \tag{1.30}$$

where $h = h(x)$ is a height profile of the terrain, in this case the ridge. and that $h(x) \to 0$ as $x \to \lambda$. u' is the horizontal and w' vertical velocity fluctuation, l is a horizontal length scale and it must be true that $l \geq \lambda$. The second equality in 1.30 assumes that all of the drag is transported upwards from the orography in the form of a vertical flux of horizontal wave momentum (assuming strictly vertical propagation of OGWs as is the case for the traditional OGW parameterization schemes) - shortly momentum flux. In x-direction, it can be generally defined as

$$\tau_x = -\overline{\rho} c_{gz} \frac{E_w}{\hat{\omega}} k, \tag{1.31}$$

where E_w is the total energy of the gravity wave. However, momentum flux is also one of the so-called stress terms that emerge in the equations of motion after application of the Reynolds decomposition

$$\begin{aligned} u &= \overline{u} + u', \\ w &= \overline{w} + w'. \end{aligned} \tag{1.32}$$

Then, written in the form of Reynolds stress the momentum flux is defined as

$$\tau_x = -\overline{\rho}\left(1 - \frac{f^2}{\hat{\omega}^2}\right)\overline{u'w'}, \tag{1.33}$$

where f is in approximation usually taken to be 0. As steady, undissipated OGWs propagate upwards, the horizontal momentum is carried with them up until the point where they dissipate. At that point, the momentum gets deposited causing acceleration or deceleration to the mean flow. This force that is exerted on the mean flow can be for purposes of models expressed as

$$F_x = \frac{\epsilon}{\overline{\rho}}\frac{\partial \tau_x}{\partial z}, \tag{1.34}$$

where ϵ is the efficiency. We call this wave-induced force and it can be used as the external force in 1.16a. Similarly defined F_y can be then used in 1.16b.

Dissipation of waves occurs through the turbulence generation arising from various instabilities. The main processes connected with the OGW breaking in the middle-atmosphere is the convective instability and dynamical instability connected with the background wind shear.

2. Parameterizations

2.1 Reasoning behind the parameterizations

A significant part of the orography remains unresolved in the current general circulation models (GCMs), but also in numerical weather prediction models. Since the effects of the subgrid-scale orography have been shown in the literature to be crucial for many aspects of the model dynamics [Eichinger et al., 2020], they need to be artificially supplemented to the models, i.e. parameterized. This concerns also the part of the drag that is propagated by OGWs and deposited especially in the middle-atmosphere.

Current OGW parametrization schemes traditionally comprise many aspects of the sub-scale orography effects on the flow, but here our main focus will be on the part of the schemes accounting for vertically propagating OGWs and the resulting orographic gravity wave drag (OGWD). For parameterizing this process, the schemes employ a lot of simplifications, such as assumption about OGW propagation (strictly vertical), sourced wave modes, instabilities and others. This inevitably introduces additional uncertainties (hard to quantify) in the models.

We illustrate the basic concept of OGW parametrizations following the pioneering work of Pierrehumbert [1986], starting with a scale analysis of the problem to get an estimate when is the wave momentum flux deposited. Consider a terrain obstacle, such as a mountain with the maximum height h, and a wind with constant wind speed U that arrives on the obstacle, then we can non-dimensionalize the system with following. Horizontal distances by L - half of the with of the obstacle, in hydrostatic approximation vertical by U/N and time by L/U, to find that the problem is characterized with two non-dimensional numbers - an inverse Froude number

$$F_i = \frac{Nh}{U}, \tag{2.1}$$

where N is the Brunt-Väisälä frequency. And a nondimensional measure of vertical motions

$$b = \frac{NL}{U}. \tag{2.2}$$

If $b >> 1$, we can use the hydrostatic approximation and F_i solely characterises the problem. So far we assumed the wave propagates conservatively. However, if the inverse Froude number, shortly just Froude number, is larger than the critical value, convective breaking occurs and some of the horizontal momentum that was to be carried higher up, is then deposited. Rest of the momentum is further transported vertically by residual waves, although at that point it is limited. For smooth, symmetric mountains the convective instability is expected to occur at approximately $F_c \approx 0.8$. However, this critical number can be different due to a wide range of conditions [Bacmeister and Pierrehumbert, 1998]. For example, in case of smaller b, for instance when the obstacle is narrower, the value of F_c is larger. Up to this point we considered only constant N and U close to the surface, but wave breaking can occur at any altitude when the amplitude of the wave exceeds critical value.

So now we take into account variance of N and U with height. With this we locate other levels of wave breaking and consequently depositioning of the

momentum flux and the resulting drag at this level. For this purpose we define a saturation flux as the maximum amount of momentum flux that can be propagated vertically without breaking of the wave. When the momentum flux is larger than this saturation value and consequently wave breaking occurs, some of the momentum flux is deposited at this level. This is the so-called (and widely used) saturation hypothesis [Lindzen, 1981].

To find the threshold for saturation we use 1.30, noting that the sign is not relevant in the estimation of the flux. So for the maximum momentum flux over length l we get

$$\tau_s = \int_{-\frac{l}{2}}^{\frac{l}{2}} \overline{\rho} u' w' \, \mathrm{d}x \approx \overline{\rho}[u'][w']l, \tag{2.3}$$

where $[u']$ and $[w']$ are typical magnitudes of velocities for a wave. As L is characteristic horizontal scale of a wave, we will say that D is a vertical one. Assuming periods of vertical and horizontal movements are bound together, we can then say that $[w'] \approx (D/L)[u']$. The magnitude of the zonal wind fluctuations reaches $[u'] = U$ during the breaking. Now we can substitute those terms to 2.3 and for saturation flux we get

$$\tau_s = \rho U^2 D \alpha. \tag{2.4}$$

$\alpha \propto 1$ stands for dimensionless constant depending on the shape of the obstacle. However, the vertical scale is a complicated non-local function of the flow. At this point, we have to assume that the background flow characteristics are only slowly varying in the vertical over the wavelength. In the hydrostatic limit we can once again estimate D locally as $D = U(z)/N(z)$ and finally rewrite the estimate of saturation flux as

$$\tau_s = \frac{\rho U^3 \alpha}{N}. \tag{2.5}$$

Considering τ is not changing before wave breaking occurs the vertical profile of τ_s can be used for estimation of the breaking level. As the density decreases exponentially, while U has to be finite, the wave breaking has to inevitably occur. Since the first wave breaking occurs quite near surface (assuming it happens), we will call this one secondary. However, the dependence of the saturation flux on the third power of U (which generally increases with height in the atmosphere) competes with the density decay and has a pronounced effect on the breaking height.

Our next step will be to estimate typical altitudes, at which the secondary wave breaking happens. In the troposphere in mid-latitudes, the wind speed generally increases with altitude until reaching the center of the upper tropospheric - lower stratospheric (UTLS) jet [Manney et al., 2011]. Although wind speed differs depending on the season (on the northern hemisphere being largest at winter) and geographical location, we can say that this local maximum of wind speed is approximately between 10 to 20 km of altitude. After that point the wind speed starts to decrease.

Let us assume that the residual momentum flux after the primary breaking is slightly less than the saturation flux. Since the momentum flux does not change, all we need for wave to break is a small decrease of τ_s at any height. What we want is then $U^3\rho < U_0^3\rho_0$, where U_0 and ρ_0 are wind speed and density at starting level. Because of the third power of wind speed this does not happen nowhere

up to the aforementioned maximum of the wind speed. Then, when the wind speed starts to decrease, the secondary wave breaking occurs and some of the momentum is deposited. This happens climatologically especially in the upper part of the UTLS jet.

With these obseravations we can formulate a minimalistic parametrization scheme that will account for the effects formed by OGWs.

2.2 Introduction of parameterization scheme

Many parameterization schemes were introduced throughout the years, and each model has a slightly different OGW parameterization, or at least uses a slightly different set-up of the tunable parameters of the scheme. Nevertheless each of these schemes follows similar basic theoretical concepts and considerations, which we will illustrate following Pierrehumbert [1986].

Firstly, we must consider how much momentum flux is propagated to the atmosphere and how it will be deposited there. As commented before, low-level OGW breaking can occur in the vicinity of the orography, however, only residual momentum flux and its deposition is considered in the following.

The wave drag terms appear in the momentum equations (Eulerian equations in a Cartesian, non-rotating frame for simplicity) after the Reynolds decomposition as a divergence of the Reynolds stress terms.

$$\rho \frac{D\vec{u}}{Dt} = -div\vec{\tau} + \rho\vec{f}, \tag{2.6}$$

where $\frac{D}{Dt}$ stands again for material derivative. We omit external forces, so $\vec{f} = 0$ and as we stated before, we assume only vertical propagation of GWs. Taking all of that into consideration, the drag force has only two components:

$$\begin{aligned} \frac{\partial u}{\partial t} + u\frac{\partial u}{\partial x} + v\frac{\partial u}{\partial y} + w\frac{\partial u}{\partial z} &= -\frac{1}{\rho}\frac{\partial \tau_x}{\partial z}, \\ \frac{\partial v}{\partial t} + u\frac{\partial v}{\partial x} + v\frac{\partial v}{\partial y} + w\frac{\partial v}{\partial z} &= -\frac{1}{\rho}\frac{\partial \tau_y}{\partial z}. \end{aligned} \tag{2.7}$$

u and v are x and y components of wind velocity (from now we will call those zonal and meridional wind). τ_x and τ_y are accordingly vertical fluxes of zonal and meridonial wave momentum defined as:

$$\begin{aligned} \tau_x &= \frac{1}{\delta x \delta y} \iint\limits_S \overline{\rho} u' w' \, \mathrm{d}x \, \mathrm{d}y, \\ \tau_x &= \frac{1}{\delta x \delta y} \iint\limits_S \overline{\rho} v' w' \, \mathrm{d}x \, \mathrm{d}y, \end{aligned} \tag{2.8}$$

where δx and δy are width and length of the grid, meaning we get average over the grid area denoted S in the integral. However, the prime quantities are unresolved by the model and they have to be estimated from the resolved quantities. For this, we return to the idealised one dimensional flow over a ridge as was in 1.30, meaning $\tau_y = 0$. Using the results from 2.1 we can estimate the sourced

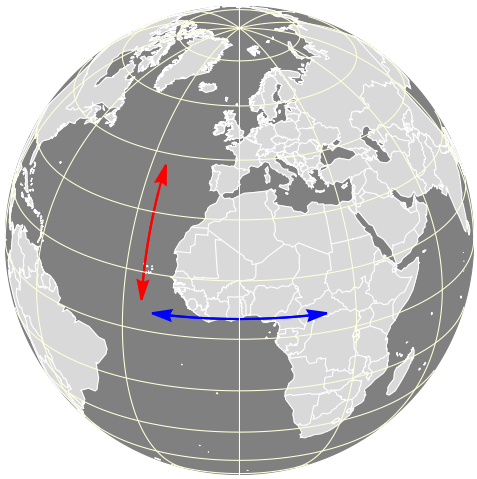

Figure 2.1: Representation of zonal wind (blue) and meridional wind (red)

momentum flux of freely propagating OGWs, τ_0, that is the residual momentum flux after the primary wave breaking as

$$\tau_0 = \frac{\rho U^3}{N\delta x} G(F_i), \tag{2.9}$$

where G is a function of the inverse Froude number.

For $F_i << 1$, i.e. a linear flow without breaking, we can say that u' and w' are proportional to the height of the ridge, then

$$G(F_i) = EF_i^2 = E\left(\frac{Nh}{U}\right)^2, \tag{2.10}$$

where E is the efficiency constant depending on the shape of the mountain. After substituting to 2.9, we get

$$\tau_0 = E\frac{\rho U N h^2}{\delta x}. \tag{2.11}$$

This is the main equation used to calculate low-level momentum flux, that is used in most models, with some small alternations. However, we must remember that this is only a core of the parameterization and that many other aspects can be employed in the OGWD parameterization schemes as we will see in the following section.

2.3 Parameterizations schemes used in models

Once we illustrated basic physical mechanisms utilised by the OGW paramaterizations, we can start with the analysis of parametrization schemes and their set-ups in different models and their effect on resulting OGWD. We will compare simulations from CMIP6 – Coupled Model Intercomparison Project Phase 6. Models at our disposal are MIROC-ES2L, MRI-ESM2, HadGEM3-GC31-LL, UKESM1-0-LL, CESM2, CanESM5, IPSL-CM6A-LR, CNRM-CM6-1 and GFDL-ESM4. These models come in different versions, but since the resulting OGWD are mostly similar between the configurations of each model we will focus on the comparison only between different models in the following. Analysed

quantity is *utendogw* $[m/s/d]$ – the tendency of eastward wind due to OGWs, which represents most frequently the deceleration of the westerly wind due to parameterized OGWD. Our motivation is that CMIP6 provides for the first time OGWD data in three dimensions allowing a detailed investigation of the OGWD distribution between the models. As we can see from example in Figure 2.2, where we compare spatial average of 9 models at pressure levels 500 hPa (≈5574 m) and 70 hPa (≈17 662 m) over the Himalayas in winter months of 2013/2014, specific values of *utendogw* can differ significantly between the models. (Note: Average height of the Himalayas is around 6000 m. However, the first chosen pressure level should be considered as representative up to the next level which is at 400 hPa so ≈7185 m).

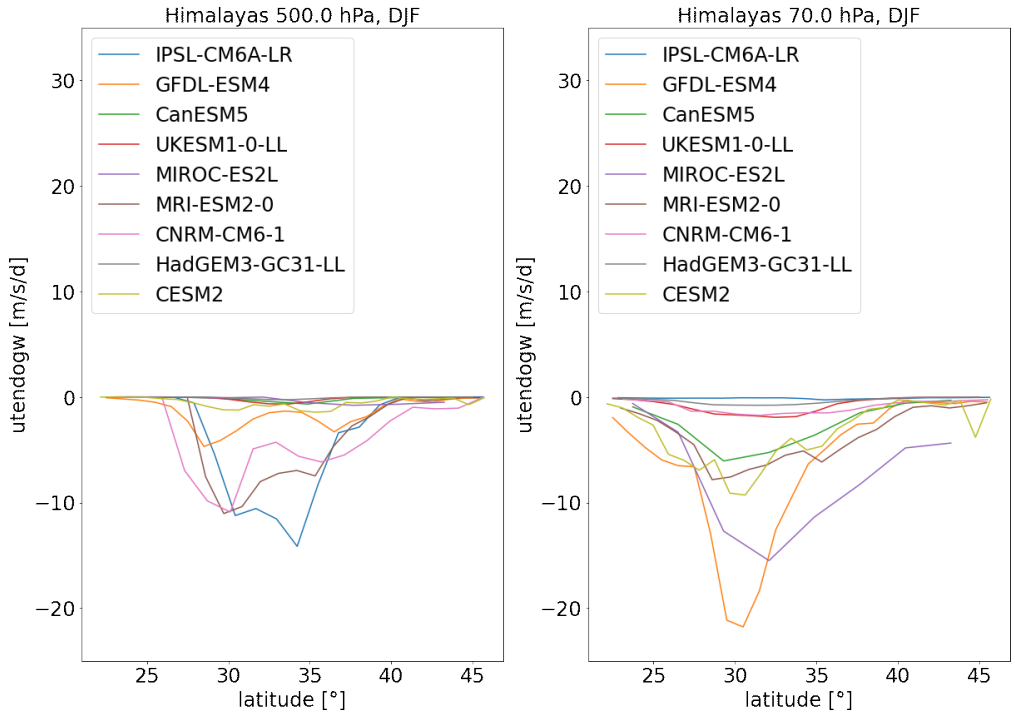

Figure 2.2: Comparison of different models at two pressure levels, the Himalayas, DJF, 2013/2014

In the following we will briefly describe the schemes used in the models, however, the official information is often limited by available papers and documentation concerning each model. Hence, in some cases, personal communication with the model developers was needed to establish the results, although we have not been able to confirm the tuning of all models. The following subsection concerns especially scheme and model - specific handling of the surface momentum flux and vertical distribution controlling parameters, such as F_c, as well as considerations of the wave blocking, low-level breaking and anisotropy of the topography. In some schemes F_c, as we defined it, is replaced by other constant which represents wave blocking or breaking limits. We adjusted them in our description to have a continuous definitions, which are alas in the accordance with the original definition and setting in the schemes.

2.3.1 MIROC-ES2L

Model with OGWD parametrization scheme based on McFarlene [1997] and with nominal horizontal resolution of 500 km. Firstly, the surface momentum flux at a reference level, σ^r, is defined as

$$\vec{\tau}(\sigma^r) = \vec{\tau}_0 = -E\frac{\kappa_e}{2}h_e^2\rho_0 N_0 \vec{U_0}, \tag{2.12}$$

with $\sigma^r = \frac{p_r}{p_s}$, where $p_{r/s}$ is the pressure at height r and at the surface respectively. $\vec{U}$ is the horizontal wind velocity, κ_e is a representative horizontal wavenumber, h_e is the effective height, which determines the wave amplitude limited by F_c and is defined as $h_e = min(2S_d, F_cU_0/N_0)$, with S_d being topography deviation specific for each grid. All terms indexed by 0 are taken at the reference level. E is an efficiency parameter always lower than one. $E\kappa_e/2$ taken together present a tunable parameter which we denote K. And as we can see, it corresponds with 2.11, so that $1/\delta x = \kappa_e/2$.

Vertical distribution of the momentum flux follows the saturation hypothesis, and we can write the vertical profile of the momentum flux as

$$\vec{\tau}(\sigma) = \vec{\tau}_0 \left(\frac{A(z)}{h_e}\right)^2 \frac{\rho N U}{\rho_0 N_0 U_0}. \tag{2.13}$$

Where wind speed U is a projection of background winds to the direction of the low level wind ($U = \vec{U} \cdot \vec{U}_0/|\vec{U}_0|$) and $A(z)$ is the wave amplitude at height z. The amplitude varies with altitude, however, it is constrained to be less than the critical value of convective overturning, $A(z) \leq F_cU/N$. If the amplitude does exceed this value, momentum is deposited in accordance with the saturation hypothesis. Saturation momentum flux is equal to 2.13 after taking $A(z) = F_cU/N$.

This scheme employs wave blocking, but it does not take into account possible low-level breaking. Parameters in this scheme have following values, $F_c = 0.707, K = 8 \times 10^{-6} m^{-1}, \sigma^r = 0.985$, but we do not have confirmed that these are the parameters used in the analysed simulation.

2.3.2 MRI-ESM2

This model uses the scheme introduced by Iwasaki et al. [1989] and it has a nominal horizontal resolution of 100 km. It is similar with the previous version of the model MIROC-ES2L, but in the updated scheme two monocromatic modes of OGWs are launched instead of one, which is used in most of the models. First type is to account for effects of waves with $\lambda \sim$100 km – type A, with the main influence in the stratosphere. Second type is to account for effects of short waves with $\lambda \lesssim$10km – type B with the main influence in the troposphere.

The momentum at the reference level is defined in the same way as 2.12, but this time we need to distinguish between the type A and B of the waves. For each type, different reference level is chosen.

$$\vec{\tau_{0i}}(\sigma_i^r) = -Kh_{ei}^2\rho_{0i}N_{0i}\vec{U}_{0i}, \tag{2.14}$$

where all variables are set according to σ^r and h_e is defined similarly as in McFarlene [1997] - $h_{ei} = min(S_{di}, 0.5F_cU_{0i}/N_{0i})$. S_{dA} is defined as the standard

deviation and $S_{dB} = 0.5(h_{max} - h_{min})$. Note the factor 0.5 in the definition of effective height. In Iwasaki et al. [1989] it is said to be due to the vertical dropping of flow over sinusoidal terrain. This drop should be twice the length of the wave amplitude.

Tunable parameter K is set to 2×10^{-5} for type A and 5×10^{-5} for type B. F_c is in this scheme tuned separately for wave blocking $F_c = 0.67$ and for amplitude limitation concerning saturation hypothesis $F_c = 1$. Other parameters are $\sigma_A^r = 0.9$ and $\sigma_B^r = 0.97$. However, these parameters were not confirmed for the analysed simulation. Note, that reference level of type B is set lower. This is based on the assumption that shorter waves are formed at lower altitudes.

Vertical evolution of drag for type A follows Palmer et al. [1986] and since it again follows the saturation hypothesis, it will not be further described here. For type B it is defined as

$$\vec{\tau}_B(\sigma) = \begin{cases} 0 & \sigma_B \leq 0.3, \\ \vec{\tau}_B(\sigma_B^r)\frac{(\sigma-0.3)^2}{0.7^2} & \sigma_B > 0.3. \end{cases} \tag{2.15}$$

Type B waves are mostly reflected by the upper troposphere downward to the surface where they can be again reflected until they dissipate. As we can see, the momentum flux is greater as we go lower, with $\sigma = 0.3$ being around 9 km, so in the upper troposphere. Parameterization of effects of short waves is not usual in other schemes. Drag from low-level breaking is not considered.

2.3.3 HadGEM3-GC31-LL and UKESM1-0-LL

These two models are grouped together because of the use of the same scheme defined by Webster et al. [2003]. The stability is constrained by the saturation hypothesis as in Gregory et al. [1998]. Both models have nominal horizontal resolution of 250 km. Anisotropy of the subgrid-scale orography is considered in the scheme describing a dependence of the elevation on the direction. For that reason we define ϕ_{xx}, ϕ_{xy} and ϕ_{yy} as

$$\begin{aligned} \phi_{xx} &= \left(\frac{\partial h(x,y)}{\partial x}\right)^2, \\ \phi_{xy} &= \frac{\partial h(x,y)}{\partial x}\frac{\partial h(x,y)}{\partial y}, \\ \phi_{yy} &= \left(\frac{\partial h(x,y)}{\partial y}\right)^2, \end{aligned} \tag{2.16}$$

where h is the height of the topography. This anisotropic handling of the subgrid orography should improve the resulting parameterized OGW momentum fluxes.

With this we define surface stress that accounts for the anisotropy of the orography as

$$\begin{aligned} \tau_{0x} &= -K\rho_0 N_0 u_0(\phi_{xx}\cos\chi + \phi_{xy}\sin\chi), \\ \tau_{0y} &= -K\rho_0 N_0 v_0(\phi_{xy}\cos\chi + \phi_{yy}\sin\chi), \end{aligned} \tag{2.17}$$

where τ_{0x} is the zonal component and τ_{0y} is the meridional component of the surface momentum flux and χ is the direction of the wind near the surface relative to the west.

To include wave blocking, h_e is defined similarly as in previous cases, $h_e = F_c U_0/N_0$. Finally we acquire surface OGW stress

$$\vec{\tau}_{gw} = \vec{\tau}_0 \left(\frac{h_e}{h}\right)^2, \tag{2.18}$$

which is the residual momentum flux that will be propagated upwards. The momentum that is dissipated due to low-level breaking and or blocking,

$$\vec{\tau}_b = \vec{\tau}_s - \vec{\tau}_{gw}, \tag{2.19}$$

is included in the model and is deposited uniformly up to altitude h, so it is not omitted completely. Since effects of this drag from blocking are explicitly implemented to the wind fields, this drag is limited to numerically stabilise the scheme [Walters et al., 2011]. In this scheme, the values of free parameters are recommended to be $K \sim 10^{-5}, F_c = 0.5$. However, for HadGEM3-GC31-LL, we have confirmed that Froude critical number is 0.25 and it is different for the saturation test, where it is equal to 4.

2.3.4 CESM2 and CanESM5

The models CESM2 and CanESM5 are also based on the same scheme. It is described in Scinocca and McFarlene [2000], which is building on the scheme by Lott and Miller [1997]. The models, however, have a vastly different nominal horizontal resolutions. CESM2 has 100 km and CanESM5 has 500 km. The parameterization scheme is a more elaborated one, consisting of three components. That is the scheme for freely propagating waves, for the low-level breaking and for the wave blocking. Here, we will focus on the freely propagating OGWs only.

Two waves are used to propagate the momentum flux. We will denote the momentum flux for each wave as $\vec{\tau}^+$ and $\vec{\tau}^-$, where one is the positive half of the integral from which the momentum flux is derived and the other is the negative half, i.e. one is from $(0; \pi/2)$ the other $(-\pi/2; 0)$. Values for these momentum fluxes in the model are derived from the pressure drag force from constant flow over topography. Complete derivation in Scinocca and McFarlene [2000] leads to moment fluxes as following,

$$\begin{aligned} \vec{\tau}^+ &= -\frac{\kappa^+}{2}\rho_0 N_0 \vec{U}_0 \cos\theta^+ (h_e^+)^2, \\ \vec{\tau}^- &= -\frac{\kappa^-}{2}\rho_0 N_0 \vec{U}_0 \cos\theta^- (h_e^-)^2, \end{aligned} \tag{2.20}$$

where θ is the angle that drag vector makes with x-axis, so that the cosine stands for the efficiency constant E. Effective height is defined as

$$\begin{aligned} h_e^+ &= \cos\theta^+ min(h_e, F_c U_0/N_0), \\ h_e^- &= \cos\theta^- min(h_e, F_c U_0/N_0). \end{aligned} \tag{2.21}$$

The other two components of the parameterization are too extensive to be described and beyond the scope of this thesis. However, the fact that the momentum flux for both low-level breaking and wave blocking is not omitted but redistributed is important for our comparison.

Critical Froude number for this parameterization is recommended to be $F_c = 0.707$. We could not find the value of a parameter concerning the wave length κ. It is also mentioned that this scheme underestimates surface dimensionless drag in case of $F_i \gtrsim 1$ and that in comparison with one-wave scheme it transports up to $30\% - 50\%$ more of momentum flux to the middle atmosphere.

For the analysed CanESM5 simulation we have found out from personal communication a specific choice of $F_c = 0.22$. Lower Froude critical number was employed, because 0.707 caused too much momentum flux to be transported up. Result was too much drag in northern hemisphere winter in the lower stratosphere. This caused lower values of wind than observed (Scinocca,J.,personal correspondence). For the CESM2 simulation we have confirmed from personal communication a specific setting $F_c = 1$, hence much lager than for the CanESM5 simulation.

2.3.5 IPSL-CM6A-LR

This model uses the scheme Lott [1999], which also bases on Lott and Miller [1997], with a nominal horizontal resolution of 250 km. The parameterization concerns freely propagating waves and a blocked flow. The effective height h_e is equal to

$$\int_{h_b}^{h_{max}} \frac{N}{U}\, \mathrm{d}z \leq F_c, \tag{2.22}$$

where h_b is the blocking height. Drag force from this blocked flow is distributed in levels below h_b.

Residual momentum flux is than calculated as

$$\vec{\tau} = -E(h_{max} - h_b)^2 \rho_0 N_0 \vec{U}_0 \frac{\sigma}{4S_d}(B\cos\psi^2 + C\sin\psi^2; (B-C)\cos\psi\sin\psi)), \tag{2.23}$$

where σ, ψ are a slope of the obstacle and the angle between the flow and a direction of the obstacle. B and C are constants dependable on γ, which is a measure of the anisotropy of the orography. These are as follows

$$\begin{aligned} B &= 1 - 0.18\gamma - 0.04\gamma^2 \\ C &= 0.48\gamma + 0.3\gamma^2. \end{aligned} \tag{2.24}$$

Vertical distribution of the drag is controlled by the saturation hypothesis. To account for drag from low-level wave breaking, a parameter β is introduced. The momentum flux then decays by this parameter up to the level of $850hPa$. Parameters in the scheme are not confirmed for our analysed model. In Lott [1999] they are chosen as $F_c = 1$ for blocking and $F_c \approx 2$ for saturation, $E = 1, \beta = 0.5$.

2.3.6 CNRM-CNM6-1

This model has a nominal resolution of 250 km and parts of the scheme it uses are described in Déqué et al. [1994] and Geleyn et al. [1994], with additions in Catry et al. [2008]. Brief description can be found in the article describing the whole model, Roehrig et al. [2020].

This scheme takes into consideration not only the wave breaking - dissipation, but also resonance and reflection effects. Complete vertical profile of the momentum flux is then given as

$$\vec{\tau}(z) = (\Gamma_1(z) + \Gamma_2(z) + \Gamma_3(z))\vec{\tau}_0, \tag{2.25}$$

where $\vec{\tau}_0$ is the already known surface stress and $\Gamma_1, \Gamma_2, \Gamma_3$ stand for dissipation, reflection by a neutral or unstable level, and damping or amplification by resonance, respectively. The latter two effects were not included in any other model scheme so far. Surface stress is defined as in Boer et al. [1984]

$$\vec{\tau}_0 = -K_{GW}\rho_0 N_0 h_{rms}\vec{U}_0, \tag{2.26}$$

where h_{rms} is the root-mean-square of the variance of the orography, and K_{GW} is a dimensionless tuning parameter, which can however be transcribed as $K_{GW} = Eh_{rms}/l$, where l is the typical distance between topographical features in the grid. Supposing this is the possible horizontal wavelength of OGWs, we get the same definition as we saw in some of the previous schemes.

Taking Froude number defined as $F_i(z) = N(z)h_{rms}/U(z)$ and $U(z)$ as in 2.13 we can introduce Γ_1. This gets us the vertical distribution

$$\Gamma_1(z) = max[0, \min_{z'<z}\Gamma(z')],\ \Gamma(z) = \frac{\rho(z)N(z)U(z)/F_i^2}{\rho_0 N_0\|\vec{U}_0\|/F_{i0}^2}. \tag{2.27}$$

We will not describe Γ_2 and Γ_3, meaning reflection and resonance, analytically, but we must consider their effects. Namely for Γ_2 it means greater deposition of the momentum flux in breaking levels, meaning lesser residual momentum flux in levels above it. For Γ_3 it means possible amplification or damping of stress at the breaking level depending on the scale of the vertical wavelength relative to the depth of the breaking layer.

The scheme also considers anisotropy by adjusting wind speed and wave blocking by multiplying the final momentum flux by coefficient dependent on F_c. This is supposed to enhance the drag, implying the drag is redistributed to blocking level. We have confirmed for this model, the specific choice of $F_c = 0.5$ and $K_{GW} = 1.5 \times 10^{-3}$ and as we showed before, it can be related to $h/\delta x$ or Kh in previous definitions.

2.3.7 GFDL-ESM4

This model uses a parameterization scheme by Garner [2005], as described in Zhao et al. [2018], and it has a nominal horizontal resolution of 100 km. This parameterization is based on a different physical mechanism than the previous ones. Previous schemes are guided by statistical anisotropy and height of the obstacle, whilst this one employs analytical approximation of a drag vector. The authors suggest, that it is not necessary to statistically describe anisotropy of unresolved topography. Instead, a potential χ is introduced such that $\nabla\chi = \rho_0\vec{U}'$, where $\vec{U}'$ is a perturbation of the horizontal velocity, meaning nabla is in this case only a horizontal operator.

This χ can be expressed as a function of wave numbers, or in spatial coordinates as follows

$$\chi(\vec{x}) = -\frac{\rho N}{2\pi} \iint \frac{h(\vec{x'})}{|\vec{x} - \vec{x'}|} \, \mathrm{d}x' \, \mathrm{d}y'. \tag{2.28}$$

It is said in Garner [2005] that topography can be analytically described with amplitudes of Fourier transform, so as a spectrum of possible waves, $\hat{h}(\vec{k})$, where $\vec{k}$ is only the horizontal wave vector. This can be also expressed in spatial coordinates, $h(\vec{x'})$, which is the term we see in definition of our potential.

$$\tilde{\chi} = \frac{\rho_0 N_0}{\rho N} \chi. \tag{2.29}$$

With that we define the base vertical flux of horizontal momentum or stress as

$$\vec{\tau}_0 = \frac{\rho N}{\rho_0 N_0} [\nabla \tilde{\chi} (\nabla h)^T] \vec{U}, \tag{2.30}$$

where $\nabla \tilde{\chi} (\nabla h)^T$ could be transcribed as a matrix. This matrix considers anisotropy, variance as well as the amplitude of the topography.

The parameterization scheme also considers the drag from wave blocking and deflection, where blocked layer is defined using F_c. However, the difference is that, the authors do not take the height as an average of a grid cell, but take h as a variable within each grid so that it corresponds with the assumed distribution of mountains. The drag from low-level blocking and or breaking is distributed near the surface. We can then divide the total momentum flux into the freely propagating and blocked components

$$\vec{\tau} = a_p \vec{\tau}_0 + a_b \vec{\tau}_b, \tag{2.31}$$

where a_p, a_b are considered to be tunable parameters.

Vertical distribution of the drag is then controlled by the saturation hypothesis with addition of assumed mountain distribution. Critical number is in the scheme tuned to $F_c = 0.7$, and we have confirmed this number for the analysed simulation as well. Other two parameters are $a_p = 1$ and $a_b = 5$, where the large value for low-level drag is due to the low resolution of the model.

3. Intermodel comparison of parameterized OGWD

Goal of this comparison is to primarily point out how much the resulting drag can differ between the models and parameterizations, and how much the tuning of the parameters can influence it. For some of the models we have confirmed specific values of parameters, these are (in short name) CNRM, CanESM5, CESM2, HADGEM3 and GFDL. For the rest the exact setting of the free parameters used in the analysed simulations is unknown. Although we have in some cases two models with the same parameterization, we do not have two parameterizations used in one model. Therefore, every hypothesis concerning the differences between the schemes and models is probably only a small part of the real reasoning.

3.1 Parameterized OGW drag

We will proceed with comparison of *utendogw* values from CMIP6 simulations, that are for the first time available on a 3-D grid as monthly means at 19 pressure levels, a summary of the data used is given in the attachment A.1. Note that the underlying resolution of each model is different, see attachment A.2 for the summary of specific values of resolution and other differences in datasets from CMIP6. For distribution analysis we use data from AMIP simulations. For trend analysis we use data from historical and ssp460 simulations.

For diagnosing and visualising the data we used Python. First, we checked the horizontal OGWD distribution at different pressure levels. Examples of two models are shown in Figure 3.1. All the models capture the asymmetric OGWD distribution reasonably well and we can identify the major hotspots connected with significant topography of the Earth. However, looking at the scale of the colorbar, we can already see great difference in the magnitudes of *utendogw*.

For our following analyses we chose 4 OGW hotspots, these are West America - the Rocky Mountains, South America - Southern Andes, the Himalayas and East Asia – Japan, Korea and Sichote-Aliň. They are displayed in Figure 3.2. The highlighted areas are used for spatial averaging, with specific values summarised in the attachment section A.3. In our analyses we combine a hotspot view with a zonal mean framework to give a detailed picture of the differences. In our hypotheses we focus our attention on the parameter F_c, which is known to have a large impact on the results (Webster et al. [2003], Scinocca,J. personal correspondence, Ridley,J. personal correspondence) and is used in all parameterizations. First we compare the OGWD spatially averaged over the Himalayas at different pressure levels. We choose the Himalayas in winter months, because of the climatologically largest OGWD values that can be found here. Although we use only one winter of 2013/2014 to have more clear comparison, we did also average over years 1980-2010 (not shown), that confirmed the differences between models.

Plots in Figure 3.3 show the spatially averaged OGWD from $\approx$3000 m up to $\approx$22 000 m of altitude, with average being specifically over the longitudes $70° - 105°$ from latitude of $22° - 46°$. We can clearly see two regions of more pronounced

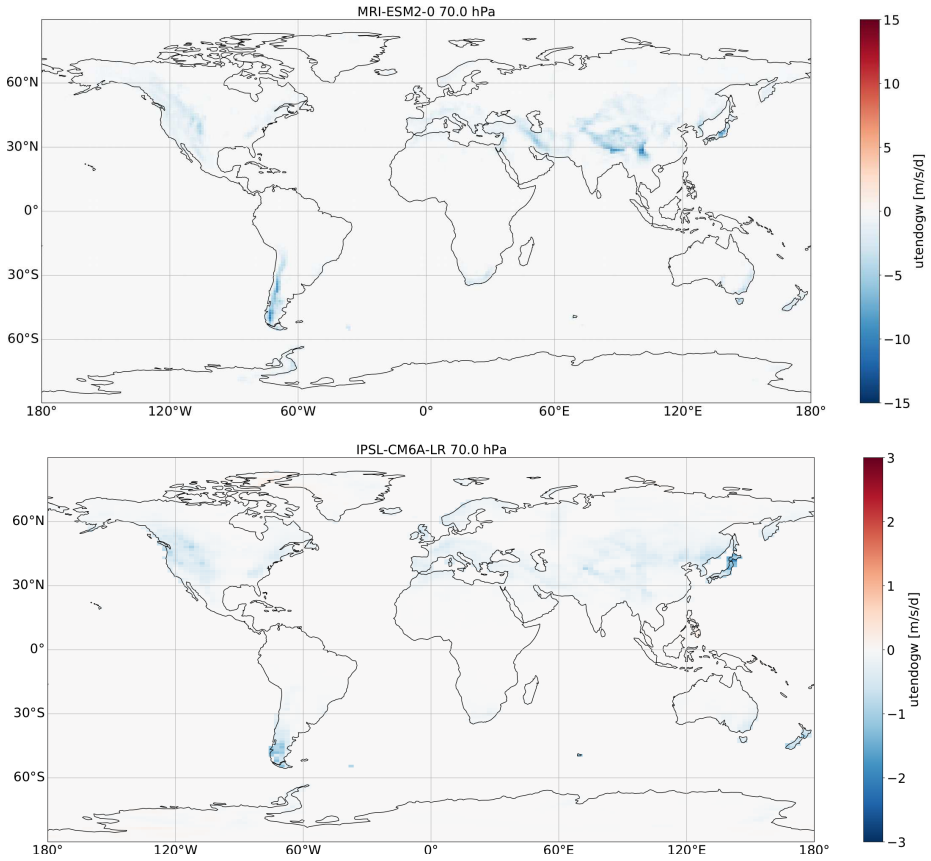

Figure 3.1: Examples of utendogw values, yearly average 2013/2014

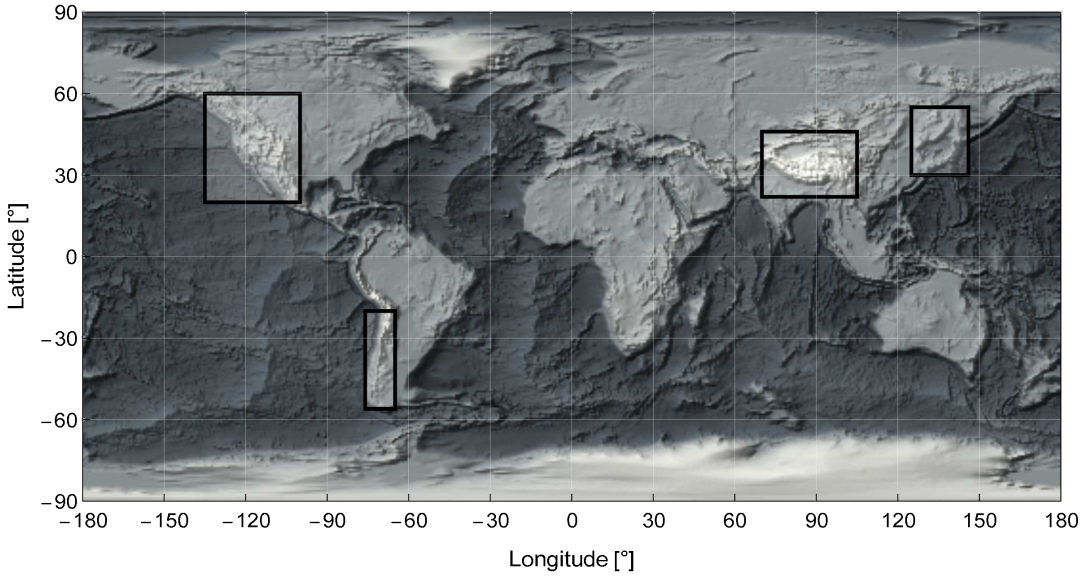

Figure 3.2: Chosen hotspot areas

values. First represents the low-level drag due to primary breaking and other low-level mechanisms at ≈5000 m and other region that represents secondary breaking at ≈ 18 000 m. This is in agreement with our estimation of breaking levels. Having verified the existence of the two regions with pronounced OGWD we make an intermodel comparison at each of those regions.

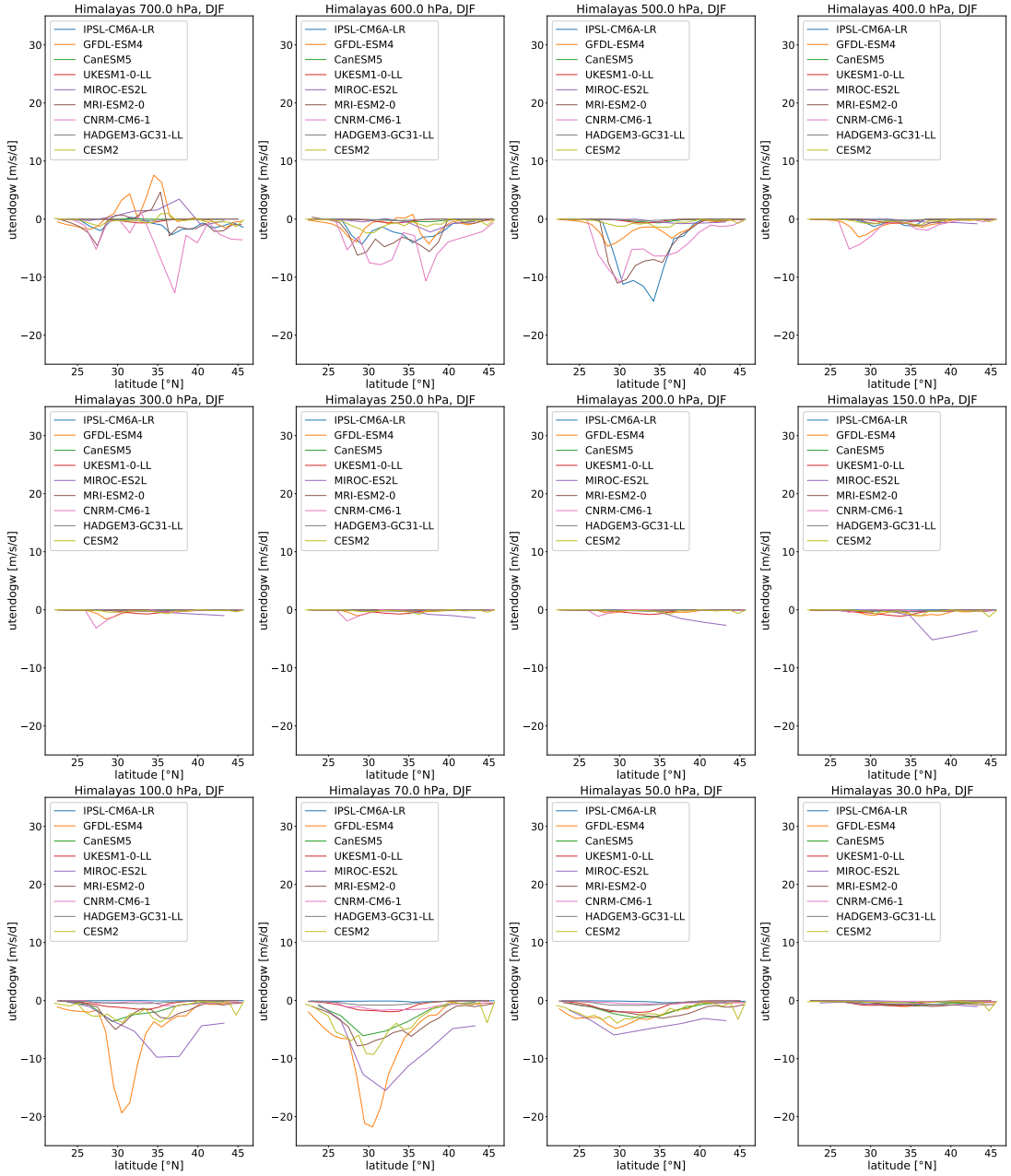

Figure 3.3: Spatial averages of *utendogw* values, the Himalayas, DJF, 2013/2014

We make this comparison for all four hotspots, in the northern hemisphere winter months, DJF - December, January, February, except for the Southern Andes where we take JJA - June, July, August - southern hemisphere winter months. Note that the levels of primary and secondary breaking can be generally different for each hotspot, because of the height of the topography and background winds. Nevertheless, we were able to identify both breaking regions for all hotspots (not shown). We will start with the first region and although we know that the drag there is not from the primary wave breaking alone, we will call this region primary breaking level for simplification.

We can see in Figure 3.4, that some models have consistently larger drag values than the other models, meaning early deposition of the momentum flux. Those models are IPSL, which shows the largest values of models for all hotspots,

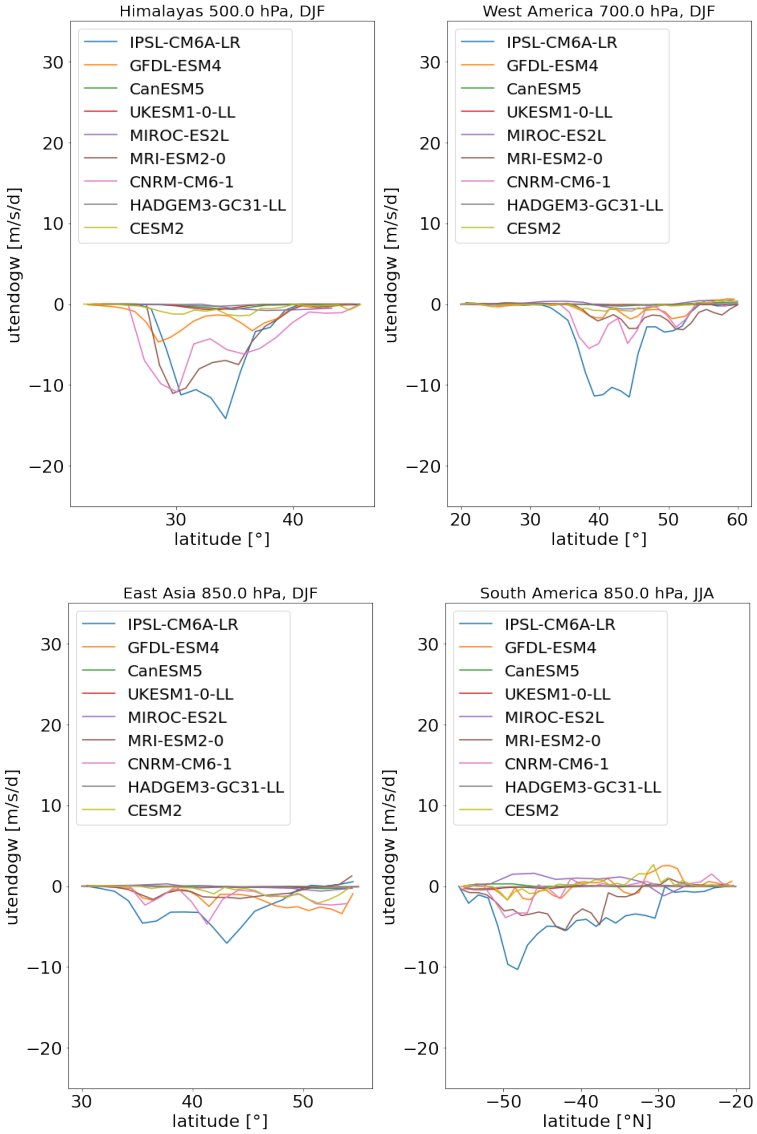

Figure 3.4: Comparison of the primary breaking level at different hotspots

CNRM, MRI, GFDL and CESM2, although the last one shows significantly smaller values. Other four models show practically zero *utendogw* values.

Explanation behind the large values of IPSL may stem from the decaying parameter β. Although it is said to cause the decay up to $850hPa$, we must remember that in the example of the Himalayas, the topography reaches much higher altitudes which influences the results. It is also in accordance with the fact, that this scheme distributes low-level drag from breaking and blocking. However, it is not quite in accordance with $F_c = 1$. We do not have confirmed this number for this model and it is possible that the tuning is different.

In case of CNRM with $F_c = 0.5$, we expect a pronounced momentum deposition due to blocking enhanced by reflection. That would be in accordance with the plot. Also, because of the small critical number, we do not expect large values of momentum flux escaping higher.

MRI does not consider drag from blocking explicitly. The explanation can probably be due to the type B waves, meaning waves with short wavelengths

that are trapped in the troposphere and enhance the low-level drag. Since we do not have established the values of the parameters for this model, it is also possible, that F_c is tuned differently.

The low-level drag values of GFDL are probably caused by the specific handling of deflection and wave blocking in the scheme and the enhancing parameter a_b. Since $F_c = 0.7$ we can still expect lot of momentum escaping higher.

Although CESM2 and CanESM5 have the same parameterization, due to complexity of the models and different tuning *untedogw* values are not completely similar. We know, that for CanESM5 the critical Froude number is definitely 0.22. Plus the fact that scheme by Scinocca and McFarlene [2000] takes into account the drag from wave blocking as well as wave breaking would imply possibly big values of low-level *utendogw*, which we do not see as pronounced in the comparison. CESM2 has $F_c = 1$, hence we would expect lower low-level drag values than for CanESM5, however we see the exact opposite. We do not have any definite explanation for that as of yet, tentatively different resolution of the models can play a role.

For MIROC, we can explain the small low level drag values by the fact, that the low-level blocking and low-level breaking is not accounted for explicitly. For this model and also CanESM5 we may also consider the influence of the very low resolution of 500 km.

HadGEM3 and also possibly UKESM1 have quite a low setting of $F_c = 0.25$, so we would expect large values of *utendogw*, which does not agree with our data. Possible explanation could be in the limitation of the low-level drag handling in their parameterization.

Next we will compare data at higher altitude at the level of secondary wave breaking. In Figure 3.5 we can see that GFDL, MRI, MIROC, CanESM5 and CESM2 show pronounced drag values. For GFDL and MIROC we could probably account this to the critical number which is for both schemes similar $F_c \approx 0.7$. It suggests that a lot of the momentum escapes from the surface, but also it is low enough so that according to the saturation hypothesis the waves will be prone to breaking. From the comparison, such a large values could indicate that those two models overestimate the drag in this region.

MRI has lower values than the two previous models. That would be in accordance with $F_c = 0.67$ for wave blocking as well as with $F_c = 1$ for saturation.

CanESM5 although with small F_c, does employ a two wave scheme, which should allow more momentum flux to be propagated further in the atmosphere. Indeed, we can see that CESM2 has at this level for all hotspots significantly larger drag values than CanESM5, which is in accordance with $F_c = 1$ used in CESM2 (higher than recommended values for this parameterization), leading us to the conclusion that the parameterized OGWD is probably overestimated in CESM2.

For a general picture, we performed also a zonal mean analysis. This is done to eliminate a possibility, that our findings can be applied only to a certain areas with more prominent topography. As we can see from Figure 3.6, the hotspot specific results hold also in a zonal mean. Globally, this is summarised for 70 hPa in Table 3.1. We choose pressure level of 70 hPa, because as we can see in Figure 3.6, there is an interference near surface above the antarctic area in several models. It shows us, that the total drag is by far largest for MIROC, followed by GFDL

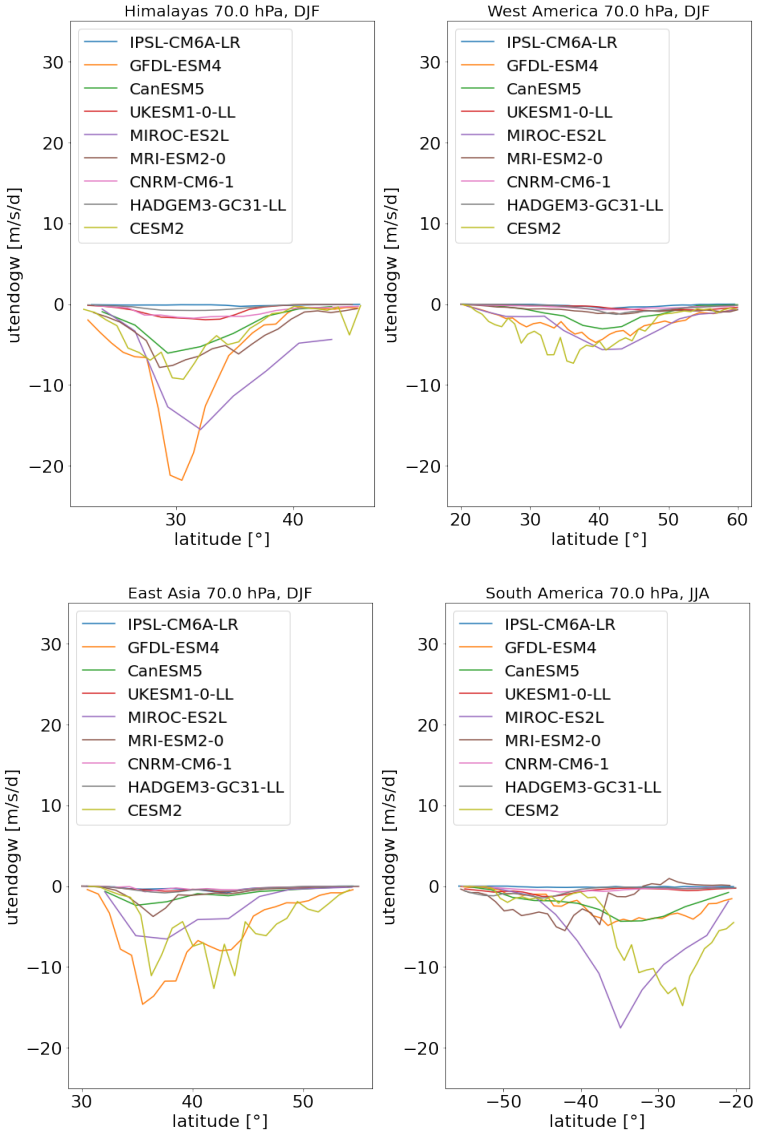

Figure 3.5: Comparison of the secondary breaking level at different hotspots

Model	
IPSL-CM6A-LR	-0.0216
GFDL-ESM4	-0.25523
CanESM5	-0.09596
UKESM1-0-LL	-0.03457
MIROC-ES2L	-0.33754
MRI-ESM2-0	-0.09878
CNRM-CM6-1	-0.02312
HADGEM3-GC31-LL	-0.03392
CESM2	-0.1946

Table 3.1: Global average of parameterized OGWD at 70 hPA

and CESM2 and that differences between CanESM5 and CESM2 are significant.

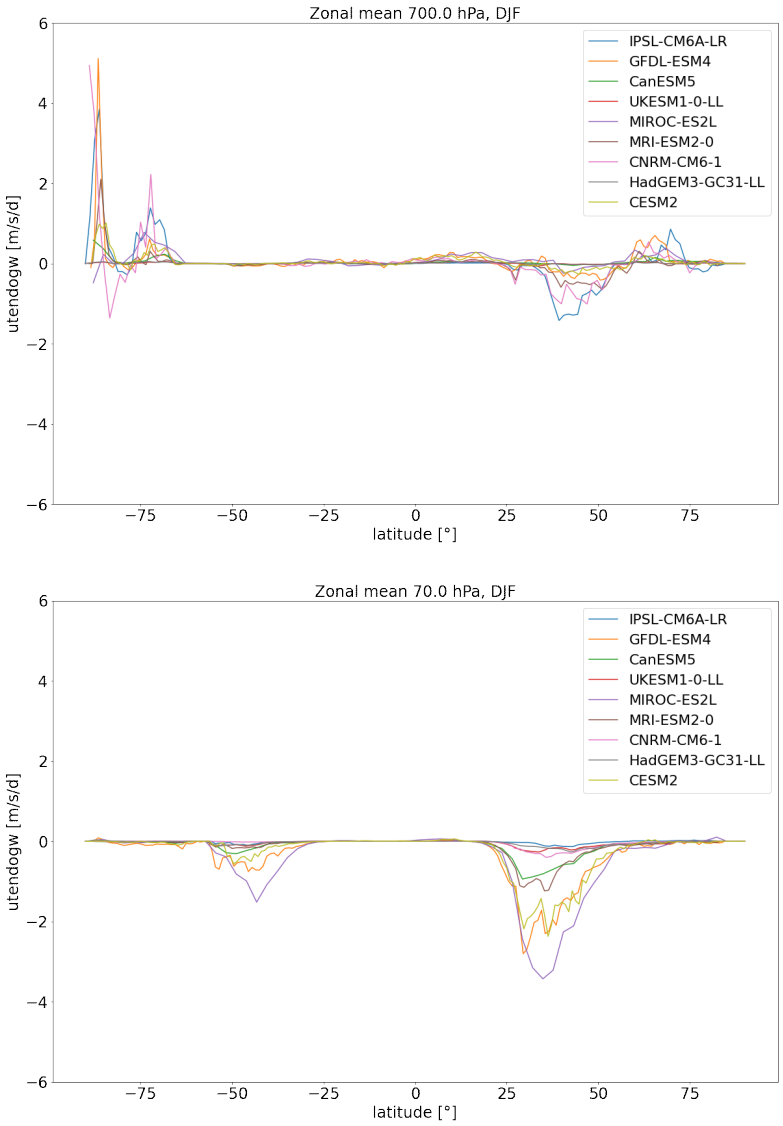

Figure 3.6: Zonal average, DJF, 2013/2014

3.1.1 Summary of the comparisons

We cannot easily say which parameterization is the best as there is not enough observational constraints and also all the mentioned explanations are only hypotheses. However, in terms of the distribution, where we expect some drag at low altitudes and some drag around 20 km we can divide the models into 4 categories. First one probably underestimates the drag in both regions. Into that category we can put both HADGEM3 and UKESM1. Since they share one parameterization, Webster et al. [2003], we could assume the problem lies here and in the combination of the used Froude numbers, which is 0.25 for blocking and 4 for saturation. However, we cannot tell why the drag is so small in the whole profile (and hence the launched momentum flux has to be small) for both models. In Figure 3.7 there is shown the distribution to the utmost level which we have available.

Second category would be models that underestimate only the low level drag compared to other models. Those models are CanESM5, MIROC and CESM2.

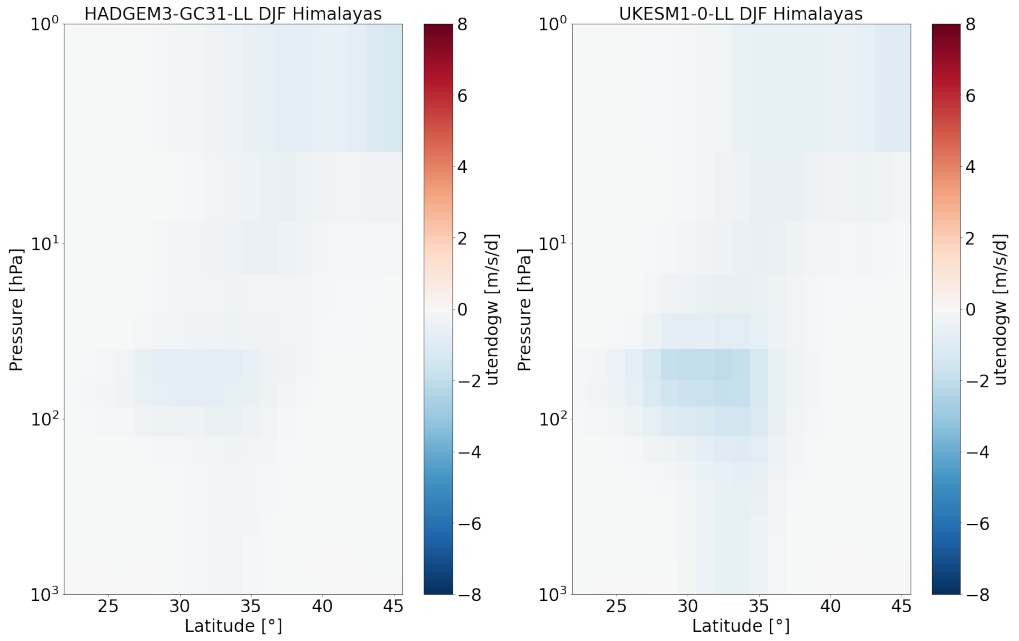

Figure 3.7: Vertical distribution, the Himalayas, DJF 2013/2014, underestimation at both breaking levels

CanESM5 and CESM2 share the same parameterization Scinocca and McFarlene

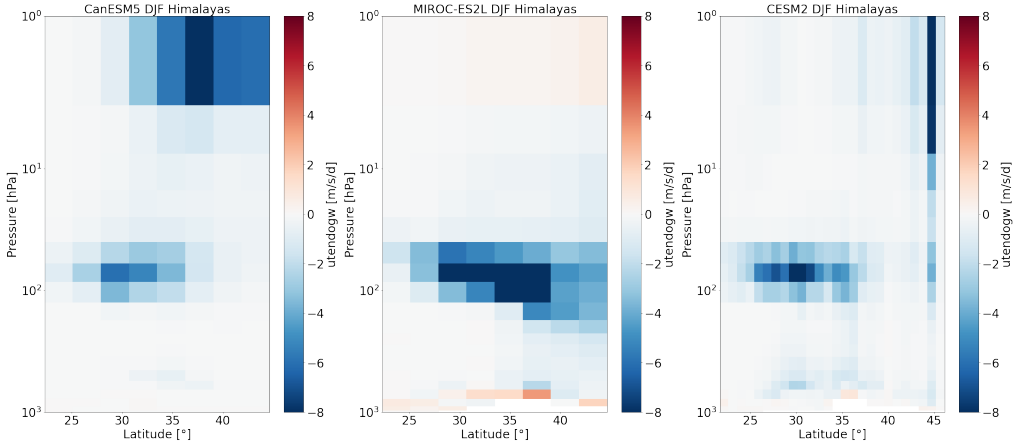

Figure 3.8: Vertical distribution, the Himalayas, DJF 2013/2014, underestimation at the primary breaking level

[2000], so it would seem that answer could lie in the scheme. Also we could not find reasoning behind the underestimation, we can say, that for the two-wave scheme low F_c is needed to limit the values at the secondary level. Otherwise large values, which we see in CESM2 with $F_c = 1$ occur. Underestimation in MIROC can be explained by not considering the drag from low-level breaking and blocking. From comparisons with other models, we can also say that using $F_c \approx 0.7$ for both blocking and saturation causes underestimation of the low level drag and possible overestimation at the secondary breaking level.

Third category underestimates the drag compared to other models at the secondary breaking level, which is the problem for IPSL and CNRM. The values of CNRM are non-zero but small, which can be caused by $F_c = 0.5$. Since we

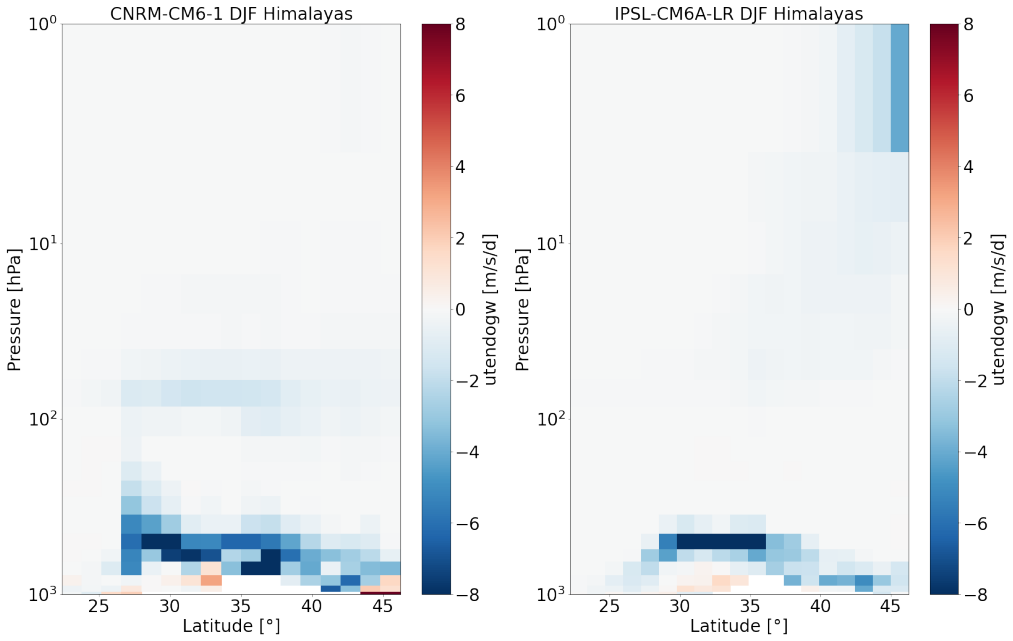

Figure 3.9: Vertical distribution, the Himalayas, DJF 2013/2014, underestimation at the secondary breaking level

can see quite large values at the surface, it would seem that by increasing F_c, more momenta would be propagated to the free troposphere and dissipate higher up. The dissipation profile seen for IPSL could be due to the decaying factor employed in the parametrization for the low-level drag and due to the $F_c \approx 2$ for the saturation. However such small values are still surprising.

Last category groups the models that give pronounced drag in both regions. In that case it seems that including short waves, as well as long ones, as we see

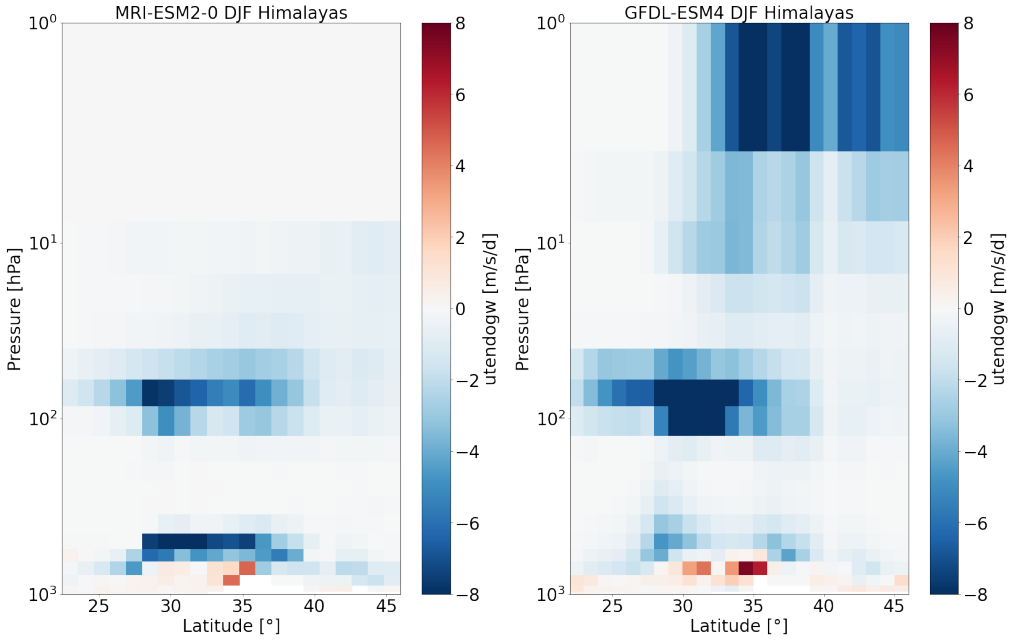

Figure 3.10: Vertical distribution, the Himalayas, DJF 2013/2014, no underestimation

in Iwasaki et al. [1989] in MRI brings good results. With $F_c = 0.67$ a lot of momentum flux escapes higher, where the saturation is defined by larger $F_c = 1$, so that there in not a large overestimation . In GFDL we can see possible overestimation of the drag from secondary breaking similarly as in MIROC, which could be connected to using $F_c \approx 7$ for both blocking and saturation.

3.2 Trends

Final part of our research concerns the possible emergence of long-term trends in the parameterized OGWD. Since this is a complex task, this section wants to merely point out how differently is drag evolving throughout the years in different models. This, of course, cannot be explained by the differences in the OGW parameterizations alone, on the opposite, we expect that the OGWD trends will differ due to the differences of the underlying background climate changes projected by the models.

We do not have historical and future simulation runs for all the models. We will show here only two, for which we have the longest time period from 1850 to 2050. Those models are MRI and IPSL. We used Mann-Kendall trend test to find and confirm trends. We conduct this test on a global average to see the changes of the total OGWD. We compute the trends for annual mean as well as seasonal mean data. We set the significance level $\alpha = 0.01$. In this test, trend is recognised if the $p-value$ is less than the significance level. This test also provides so called Mann Kendall's score. This score works on a simple principle, if the value of our variable is greater than the previous one it adds 1 to the score. If it is less than the previous value it subtracts 1, meaning larger the absolute value of the score, more prominent the trend is. Another variable is slope or so called Sen's slope which represents magnitude of the change. Following are tables with results of this test. We conducted this test on 700 hPa and 70 hPa levels. We would like to remind that the trend of increasing of *utendogw* values means lowering of the drag and the term decreasing means enhancement of the drag with time.

Test at 700 hPa - MRI-ESM2-0	Trend	p-value	Score	Slope
M-K original	no trend	0.2861	-1018	-6.53e-6
M-K original - JJA months	decreasing	0.0018	-2954	-3.63e-5
M-K original DJF months	increasing	0.0014	3052	4.06e-05
M-L seasonal test	no trend	0.4812	-2310	-3.76e-6

Table 3.2: Mann-Kendall trend test, 700 hPa, MRI-ESM2-0

Test at 700 hPa - IPSL-CM6A-LR	Trend	p-value	Score	Slope
M-K original	increasing	5.43e-11	6254	1.183e-4
M-K original - JJA months	increasing	0.0019	2942	1.08e-4
M-K original DJF months	increasing	1.79e-7	4978	1.534e-4
M-L seasonal test	increasing	1.55e-15	26138	1.197e-4

Table 3.3: Mann-Kendall trend test, 700 hPa, IPSL-CM6A-LR

Test at 70 hPa - MRI-ESM2-0	Trend	p-value	Score	Slope
M-K original	decreasing	0	-9182	-8.897
M-K original - JJA months	decreasing	4.441e-16	-7722	-5.153
M-K original DJF months	decreasing	4.8e-4	-3328	-4.742
M-L seasonal test	decreasing	0	-62696	-8.401

Table 3.4: Mann-Kendall trend test, 70 hPa, MRI-ESM2-0

Test at 70 hPa - IPSL-CM6A-LR	Trend	p-value	Score	Slope
M-K original	increasing	0	9938	2.677
M-K original - JJA months	no trend	0.967	40	1.292
M-K original DJF months	increasing	7.572e-14	7130	2.844
M-L seasonal test	increasing	0	47940	2.241

Table 3.5: Mann-Kendall trend test, 70 hPa, IPSL-CM6A-LR

We can see, that the altogether trends are rather opposite when comparing the models. This differences are important to recognise, for they could tell us how the OGWs react to different forcings and time evolution of the models.

Conclusion

OGWs are a naturally occurring an ubiquitous phenomenon in the atmosphere. They exist on a wide range of horizontal as well as vertical scales and have important dynamical influence on the atmosphere, which is related to a drag force resulting from their dissipation. During the dissipation, the momentum flux propagated in the form of OGWs to the atmosphere from the surface is deposited in the breaking regions. Due to the low resolution of the current global climate models, effects of unresolved OGWs (majority of their spectrum) must be parameterized. The goal of this thesis was to compare parameterized OGW drag from different models.

In this thesis, we first described OGWs analytically and illustrated the mechanism of their formation. In the second chapter of the thesis, we sketched the basic concept of the OGW parameterization schemes. We reviewed and briefly described 7 different parameterizations which are used in 9 CMIP6 model simulations analysed in this thesis. The underlying physical mechanisms and tuning of the free parameters were detailed for each scheme, in some cases using unique (unpublished) information established from personal communication with the model developers. We then took the drag data from the CMIP6 simulations and performed an intermodel comparison of the magnitude and distribution of the drag. We focused on four different hotspots around the globe, that show the largest values of the drag.

Differences between the individual models are greater than initially expected. From the theory we expected to see two pronounced regions of OGW breaking. This was however not the case for all of the simulations. Some models showed either too large or too little dissipation near the surface which sometimes consequently leads to either too small or too great values of drag at the secondary breaking level. We also indicated two models that most likely strongly underestimate the drag in both breaking regions. To summarise the results we grouped the simulations into four categories based on the OGWD magnitude and vertical distribution. Although the reasons of these differences cannot be identified with certainty, for each model and OGW parameterization set-up we provided a tentative explanation for its performance, informed by the physics and tuning of each scheme.

Finally we have chosen two model simulations and analysed the long-term evolution of OGWD. Also for the trends we have found large differences between the simulations. However, the reason for the difference cannot be most likely attributed to the different parameterization schemes as the long-term drag changes are influenced by the co-occurring changes in the background fields of the models that enter the parameterization and are not identical among the simulations.

This thesis is unique as such a systematic inter-model comparison of OGW parameterizations and the resulting drag was never conducted before in the literature to the authors knowledge. The main message is that there are unexpectedly large differences between the models and different schemes, showing that the state-of-the-science handling of the parameterized OGWD is still imperfect, which then adds an undesirable portion of uncertainty to the future climate projections. This can be most problematic esp. for chemistry-climate models that

rely on a precise information on transport processes, or for assessments of future regional circulation changes that are both very sensitive to localized nuances of the model dynamics.

This thesis also indicated a need for a follow up research that is to date also missing in the literature, namely an inter-comparison of different OGW parameterizations applied in one selected model for experimentation with the tuning parameters to get a clear idea about the actual performance of the different schemes.

Bibliography

D. G. Andrews. *An Introduction to Atmospheric Physics*. Cambridge University Press, Cambridge, UK, 2000. ISBN 0-521-62051-1.

J.T. Bacmeister and R.T. Pierrehumbert. On high-drag states of nonlinear stratified flow over an obstacle. *J Atmos Sci*, 45(1):63–80, 1998. doi: 10.1175/1520-0469(1988)045⟨0063:OHDSON⟩2.0.CO;2.

G.J. Boer, N.A . McFarlane, R. Laprise, J.D. Henderson, and J.-P. Blanchet. The Canadian Climate Centre spectral atmospheric general circulation model. *Atmosphere-Ocean*, 22(4):397–429, 1984. doi: 10.1080/07055900.1984.9649208.

B. Catry, J.-F. Geleyn, F. Bouyssel, J. Cedilnik, R. Brozkova, and M. Derkova. A new sub-grid scale lift formulation in a mountain drag parameterisation scheme. *Meteorologische Zeitschrift*, 17:193–208, 2008. doi: 10.1127/0941-2948/2008/0272.

M. Déqué, C. Dreveton, A. Braun, and D. Cariolle. The ARPEGE/IFS atmosphere model: A contribution to the French community climate modellin. *Climate Dynamics*, 10:249–266, 1994. doi: 10.1007/BF00208992.

R. Eichinger, H. Garny, P. Šácha, J. Danker, S. Dietmüller, and S. Oberländer-Hayn. Effects of missing gravity waves on stratospheric dynamics; part 1: climatology. *Clim Dyn*, 54:3165–3183, 2020. doi: 10.1007/s00382-020-05166-w.

D.C. Fritts and Alexander. Gravity wave dynamics and effects in the middle atmosphere. *Reviews of Geophysics*, 41(1), 2003. doi: 10.1029/2001RG000106.

S.T. Garner. A Topographic Drag Closure Built on an Analytical Base Flux. *J Atmos Sci*, 62:2302–2315, 2005. doi: 10.1175/JAS3496.1.

J. F. Geleyn, E. Balize, P. Bougeault, P. Deque, V. Ivanovici, A. Joly, L. Labbé, J.-P. Piédelièvre, J.-M. Piriou, and J.-F. Ryer. Atmospheric parametrization schemes in Meteo- France's ARPEGE NWP model. *Conference paper, Seminar on Parametrization of Sub-grid Scale Physical Processes, 5-9 September 1994*, 1994.

D. Gregory, G.J. Shutts, and J.R. Mitchell. A new gravity-wave-drag scheme incorporating anisotropic orography and low-level wave breaking: Impact upon the climate of the UK Meteorological Office Unified Model. *Quart J Roy Meteor Soc*, 124:463–493, 1998. doi: 10.1002/qj.49712454606.

T. Iwasaki, S. Yamada, and K. Tada. A Parameterization Scheme of Orographic Gravity Wave Drag with two different vertical partitionings part i: Impacts on medium-range forecasts. *J Meteor Soc Japan*, 69:11–27, 1989. doi: 10.2151/jmsj1965.67.1_11.

R.S. Lindzen. Turbulence and stress owing to gravity wave and tidal breakdown. *J Geophys Res*, 86(C10):9707–9714, 1981. doi: 10.1029/JC086iC10p09707.

F. Lott. Alleviation of stationary biases in a GCM through a mountain drag parameterization scheme and a simple representation of mountain lift forces. *Mon Weather Rev*, 127:788–801, 1999. doi: 10.1175/1520-0493(1999)127Âą0788:AOSBIA⟩2.0.CO;2.

F. Lott and M.J. Miller. A new subgrid-scale orographic drag parametrization: Its formulation and testing. *Quart J Roy Meteor Soc*, 123:101–127, 1997. doi: 10.1002/qj.49712353704.

G. Manney, M. Hegglin, W. Daffer, M. Santee, E. Ray, S. Pawson, M. Schwartz, C. Boone, L. Froidevaux, N. Livesey, W. Read, and K. Walker. Jet characterization in the upper troposphere/lower stratosphere (UTLS): Applications to climatology and transport studies. *Atmospheric Chemistry and Physics Discussions*, 11(1):6115–6137, 2011. doi: 10.5194/acp-11-6115-2011.

N.A. McFarlene. The effect of orographically excited gravity wave drag on the general circulation of the lower stratosphere and troposphere. *J Atmos Sci*, 59: 371–386, 1997. doi: 10.1175/1520-0469(1987)044⟨1775:TEOOEG⟩2.0.CO;2.

C. J. Nappo. *An Introduction to Atmospheric Gravity Waves*. Volume 85, INTERNATIONAL GEOPHYSICS SERIES. Academic Press, San Diego, USA, 2002. ISBN 978-0-12-514082-9.

T.N. Palmer, G.J. Shutts, and R. Swinbank. Alleviation of a systematic westerly bias in general circulation and numerical weather prediction models through an orographic gravity wave drag parameterization. *Quart J Roy Meteor Soc*, 112:1001–1039, 1986. doi: 10.1002/qj.49711247406.

R.T. Pierrehumbert. An essay on the parameterization of orographic gravity wave drag. *Conference paper, Seminar/Workshop on Observation, Theory and Modelling of Orographic effects. Seminar: 15-19 September 1986, Workshop: 19-20 September 1986*, 1986.

Z. Procházková. On the Internal Gravity Wave - Atmospheric Circulation Interaction. Master's thesis, Charles University, Faculty of Mathematics and Physics, Prague, Czech Republic, 2021.

R. Roehrig, I. Beau, D. Saint-Martin, A. Alias, B. Decharme, J.-F. Guérémy, A. Voldoire, A. Y. Abdel-Lathif, E. Bazile, S. Belamari, S. Blein, D. Bouniol, Y. Bouteloup, J. Cattiaux, F. Chauvin, M. Chevallier, J. Colin, H. Douville, P. Marquet, M. Michou, P. Nabat, T. Oudar, P. Peyrillé, J.-M. Piriou, D. Salas y Mélia, R. Séférian, and S. Sénési. The CNRM Global Atmosphere Model ARPEGE-C limat 6.3: Description and evaluation. *Journal of Advances in Modeling Earth Systems*, 12, 2020. doi: 10.1029/2020MS002075.

P. Sacha, A. Kuchar, R. Eichinger, P. Pisoft, C. Jacobi, and H.E. Rieder. Diverse Dynamical Response to Orographic Gravity Wave Drag Hotspots—A Zonal Mean Perspective. *Geophysical Research Letters*, 48(13), 2021. doi: 10.1029/2021GL093305.

J.F. Scinocca and N.A. McFarlene. The parametrization of drag induced by stratified flow over anisotropic orography. *Quart J Roy Meteor Soc*, 126:2353–2393, 2000. doi: 10.1002/qj.49712656802.

D. N. Walters, M. J. Best, A. C. Bushell, D. Copsey, J. M. Edwards, P. D. Falloon, C. M. Harris, A. P. Lock, J. C. Manners, C. J. Morcrette, M. J. Roberts, R. A. Stratton, S. Webster, J. M. Wilkinson, M. R. Willett, I. A. Boutle, P. D. Earnshaw, P. G. Hill, C. MacLachlan, G. M. Martin, W. Moufouma-Okia, M. D. Palmer, J. C. Petch, G. G. Rooney, A. A. Scaife, and K. D. Williams. The Met Office Unified Model Global Atmosphere 3.0/3.1 and JULES Global Land 3.0/3.1 configurations. *Geoscientific Model Development*, 4(4):919–941, 2011. doi: 10.5194/gmd-4-919-2011.

S. Webster, A.R. Brown, D.R. Cameron, and C.P. Jones. Improvements to the representation of orography in the Met Office Unified Model. *Quart J Roy Meteor Soc*, 129:1989–2010, 2003. doi: 10.1256/qj.02.133.

M. Zhao, J.-C. Golaz, I. M. Held, H. Guo, V. Balaji, R. Benson, J.-H. Chen, X. Chen, L. J. Donner, J. P. Dunne, K. Dunne, J. Durachta, S.-M. Fan, S. M. Freidenreich, S. T. Garner, P. Ginoux, L. M. Harris, L. W. Horowitz, J. P. Krasting, A. R. Langenhorst, Z. Liang, P. Lin, S.-J. Lin, S. L. Malyshev, E. Mason, P. C. D. Milly, Y. Ming, V. Naik, F. Paulot, D. Paynter, P. Phillipps, A. Radhakrishnan, V. Ramaswamy, T. Robinson, D. Schwarzkopf, C. J. Seman, E. Shevliakova, Z. Shen, H. Shin, L. G. Silvers, J. R. Wilson, M. Winton, A. T. Wittenberg, B. Wyman, and B. Xiang. The GFDL Global Atmosphere and Land Model AM4.0/LM4.0: 2. Model Description, Sensitivity Studies, and Tuning Strategies. *Journal of Advances in Modeling Earth Systems*, 10(3): 735–769, 2018. doi: https://doi.org/10.1002/2017MS001209.

List of Figures

List of Abbreviations

GWs gravity waves 3

OGW orographic gravity wave iii

OGWD orographic gravity wave drag 13

A. Attachments

A.1 First Attachment

Pressure levels [hPa]:	1000	925	850	700	600	500	400	300	250	200
	150	100	70	50	30	20	10	5	1	
Experiment ID:	distribution: amip				trends: historical + ssp460					
Table ID:	Emon		Frequency:		Monthly					

A.2 Second Attachment

Model	Hor. res. [km]	Variant label for CMIP6	Param. scheme
CanESM5	500	r1i1p1f1	Scinocca and McFarlene [2000]
CESM2	100	r1i1p1f1	Scinocca and McFarlene [2000]
CNRM-CM6-1	250	r1i1p1f2	Déqué et al. [1994],Geleyn et al. [1994]
GFDL-ESM4	100	r1i1p1f1	Garner [2005]
HADGEM3-GC31-LL	250	r1i1p1f3	Webster et al. [2003]
IPSL-CM6A-LR	250	r2i1p1f1	Lott [1999]
MIROC-ES2L	500	r1i1p1f2	McFarlene [1997]
MRI-ESM2-0	100	r1i1p1f1	Iwasaki et al. [1989]
UKESM1-0-LL	250	r1i1p1f4	Webster et al. [2003]

A.3 Third Attachment

Hotspot	Latitude	Longitude
The Himalayas	22°N - 46°N	70°E - 105 °E
West America	20°N - 60°N	100°W - 135°W
East Asia	30°N - 55°N	125°E - 146 °E
South America	20°S - 56°S	65°W - 76°W